Physical Modeling of Progressive Damage and Failure of Wood-Frame Coastal Residential Structures Due to Surge and Wave Forces

Sean Duncan[a], Daniel Cox[a], Andre R. Barbosa[a], Pedro Lomónaco[b], Hyoungsu Park[c], Mohammad S. Alam[a], Caileen Yu[d]

[a] School of Civil and Construction Engineering, Oregon State University, Corvallis, OR, 97331, USA
[b] O.H. Hinsdale Wave Research Laboratory, Oregon State University, Corvallis, OR, 97331, USA
[c] Department of Civil and Environmental Engineering, University of Hawai'i at Manoa, Honolulu, HI, 96822, USA
[d] Civil and Environmental Engineering, University of California, Berkeley, Berkeley, CA, 94720, USA

Abstract

A physical model study was performed to examine the forces and response of 1:6 scale wood-frame coastal residential structures subjected to storm surge and waves. An on-grade and an elevated specimen were tested and exposed to regular waves with varying water depths and wave heights to simulate typical wave/surge conditions resulting from landfall hurricanes on low-lying barrier islands such as Hurricane Sandy that impacted the US East Coast in 2012 and Hurricane Ike that affected the US Gulf Coast in 2008. Results show that through careful design, wood-frame model specimens can be constructed to have similar strength and stiffness compared to full-scale structures. The two specimens were subjected to increasing surge and wave conditions, and the progressive damage was monitored using LiDAR. The on-grade specimen failed at a lower water level than the elevated specimen as expected. Both specimens showed failure modes consistent with the observed damage of residential structures in Ortley Beach, NJ, after Hurricane Sandy and on the Bolivar Peninsula, TX, after Hurricane Ike. The pressure distribution on the underside of the elevated structure and the resulting vertical forces on the on-grade structure were also examined in this study. The pressure distribution and the resulting vertical forces were significantly affected by water depth, wave height, and air gap. The results indicate that maximum vertical forces are positively correlated to wave height and water depth and negatively correlated to the air gap. The breaking type also affects vertical forces. Nonbreaking waves correlated to relatively small vertical forces, and waves breaking directly on the specimen correlated to peak vertical forces. Accelerometer data showed that the specimen decreased in stiffness during the tests due to progressive damage. An uplift pressure distribution

equation was developed for an elevated residential structure as a function of wave height and air gap. The equation is generally conservative when compared to other data sets. The results and data presented in this study increase the current knowledge of the interaction between waves and residential structures, which may be useful to increase the resiliency of coastal communities.

Keywords: Elevated structure; Wood-frame structures; Vertical force; Physical experiment; Wave forces; Destructive tests; Hurricane

1. Introduction

As coastal communities continue to grow and sea levels continue to rise, the risk associated with hurricanes increases. Of the five costliest hurricanes in US history, four of them have occurred between 2012 and 2017 after accounting for inflation (NOAA and NHC, 2018; Blake and Gibney, 2008). In 2005, Hurricane Katrina devastated areas of Louisiana, Alabama, and Mississippi and demonstrated that much of the infrastructure on the coast is extremely vulnerable to storm surge and wave-induced forces, including elevated structures such as bridges and parking garages (Eamon et al., 2007; Mosqueda et al., 2007; Robertson et al., 2007). Hurricane Ike, which made landfall on the Bolivar Peninsula in Texas in 2008, and Hurricane Sandy, which caused extensive damage to New York and New Jersey in 2012, brought more attention to coastal residences and their vulnerability to storm surge and wave forces (Hatzikyriakou et al., 2015; Kennedy et al., 2011; Tomiczek et al., 2013, 2017). Hurricanes Irma and Maria led to similar devastation in the US Virgin Islands and Puerto Rico (Cox et al., 2019; Prevatt et al., 2018). Research indicates that hurricanes will continue to increase in intensity and cause destruction levels of the hurricanes mentioned above (Elsner et al., 2012). Understanding the forces generated by hurricane surge and waves on coastal structures and how these structures respond is necessary to mitigate the potential damage from these foreseeable intense storms.

There are two main goals of this study:

1. The first goal is to establish a methodology to construct scaled wood-frame specimens to behave and fail under the action of wave loading similarly to their full-scale counterparts.

2. The second goal is to develop a predictive equation for the uplift pressure distribution for the elevated structure considered in this experiment.

Section 1 is an introduction and gives the motivation behind this study. In Section 2, a literature review of past research demonstrates how this study extends the current knowledge of wave-induced forces on structures. Section 3 gives the details of the experimental design and setup, including the configuration in the Directional Wave Basin at Oregon State University and summary of the design and construction of the specimens completed earlier by Burke (2018) and Karny (2018). Section 4 discusses the methods of the structural tests performed on the specimens and their calculated structural properties, including stiffness, damping ratio, and natural frequency. Section 5 provides information on the hydrodynamic tests performed in the wave basin using only regular waves and water depths informed from observed conditions during Hurricane Sandy. Section 5 also includes the time-series data of the wave gauges and acoustic-Doppler velocimeters in the wave basin and the time-series data of the load cells, pressure sensors, and accelerometers installed on the specimens to measure the wave-structure interaction. Section 6 details the results of the study, including the description of the progressive damages and failure of the specimens, the evaluation of the pressure distribution and vertical forces on the elevated specimen, and the development of a predictive uplift pressure distribution equation for the elevated specimen based on wave height and air gap. The equation is compared to data and results from previous studies such as Park et al. (2017), Tomiczek et al. (2017; 2019), and Bradner et al. (2011). Section 7 and Section 8 provide a discussion and conclusions of the study, respectively.

2. Literature Review

Current design manuals for structures built in coastal areas, such as the Coastal Construction Manual (FEMA, 2011) and ASCE 7-16 (ASCE, 2016), provide conservative equations to estimate flood loads, wave-induced forces on columns and walls, and hydrodynamic uplift due to tsunamis. Design equations have been developed for ocean and coastal structures such as offshore oil platforms and breakwaters, including the well-known Morison equation for wave loads on cylinders (Morison et al., 1950;

Sarpkaya and Isaacson, 1981) and the Goda equation for wave loads on vertical caissons (Goda, 2010, 1974). Takahashi et al. (1994) extended the Goda equations to account for impulsive breaking waves on caissons. More recently, Wiebe et al. (2014) and Tomiczek et al. (2019) modified the Goda equations (Goda, 1974, 2010) to estimate wave forces on elevated structures using scaled-laboratory tests on idealized structures. However, the studies were mainly focused on wave-induced horizontal pressure distributions and forces rather than vertical (uplift) forces or the reaction of the structure (Tomiczek et al., 2019; Wiebe et al., 2014). It is important to note that the Coastal Construction Manual lacks an equation for the vertical force caused by waves on the underside of structures.

Previous studies have attempted to develop equations for uplift for horizontal platforms, typically located in deep to intermediate water depth. Kaplan (1979) and Kaplan et al. (1995) studied offshore horizontal (flat) platforms and structural members to develop an analytical model to predict horizontal and vertical forces. Cuomo et al. (2007) developed equations for wave-induced forces, both horizontal and vertical, on jetties from a 1:25 scale laboratory experiment and compared the results to previous work. The comparisons showed that the earlier equations in Kaplan and others failed to predict measured forces of the experimental data. The new equations developed by Cuomo et al. (2007) were dependent on a dimensionless parameter that included the wave crest height, water depth, and clearance of the deck above the mean water level. The equation required multiple coefficients fitted for each structural member of the specimen and is challenging when applied to a wide range of structures (Cuomo et al., 2007). Sun et al. (2011) performed a laboratory experiment to predict uplift forces on a horizontal plate using spectral analysis of random waves.

Bradner et al. (2011) constructed a 1:5 scale bridge deck and subjected it to waves characterized by different wave heights and periods in varying depths of water based on Hurricane Ivan's surge and wave conditions in 2004. They measured horizontal and vertical forces and found that vertical forces were larger than horizontal forces on the model bridge deck by a factor of 4 to 5. They also found that wave height is the most significant determinant of wave forces, and the relationship of water depth to vertical force was more complex. They concluded that the vertical forces were the greatest when the still water level was at

the bottom of the bridge deck. From these findings, they developed predictive horizontal and vertical force equations based solely on wave height for specific inundation depth and wave periods (Bradner et al., 2011).

Although the studies mentioned above increased our understanding of the effects of vertical forces on horizontal platforms, there have been relatively few studies that consider uplift forces on elevated coastal residences in relatively shallow water. Park et al. (2017) performed a laboratory experiment where they subjected an idealized elevated specimen to hurricane type waves. Due to their unique setup, the researchers could raise and lower the specimen to study the effects of air gap on the wave and surge induced horizontal and vertical forces. As mentioned above, Tomiczek et al. (2019) compared the measured horizontal pressures from this experiment to the modified Goda equations from Wiebe et al. (2014). They showed that these equations gave conservative estimates of the wave forces and improved on the existing equations in ASCE 7-16. Park et al. (2017) and Tomiczek et al. (2019) found that the peak vertical forces occurred when the still water level was even with the base of the specimen, similar to the work of Bradner et al. (2011) and others.

Alam et al. (2020) used the specimen from the experiments of Park et al. (2017) to study horizontal and vertical pressures and forces due to solitary waves. They tested both breaking and nonbreaking wave conditions when the water depth was below the bottom elevation of the specimen and even with the bottom elevation of the specimen. The researchers found that the uplift pressure distribution on the bottom of the specimen was linearly decreasing with the greatest pressures at the front of the specimen and the smallest pressures at the back side of the specimen. The variation in vertical pressure measurements also varied significantly more for the broken wave conditions when compared to the nonbreaking wave conditions.

Another recent laboratory experiment with idealized elevated coastal structures was performed by Sogut et al. (2020). The researchers set up an array of 1:40 scale elevated structures in a two-by-three grid to measure the effects that elevation and position in the grid have on the horizontal and vertical forces on the structures when subjected to inundation and solitary waves. While the effect of the position of the structures was negligible, the vertical forces were significantly affected by the elevation of the specimens (Sogut et al., 2020). Similar to the work of Bradner et al. (2011) and Park et al. (2017), they found the

maximum vertical force occurred when the floor elevation of the structure is even with the still water level. It is noted that the experiment performed by Sogut et al. (2020) considered the forces due to solitary (tsunami-like) waves rather than modeling hurricane induced surge and wave conditions.

In addition to the need to quantify wave forces, it is also vital to understand how and when structures will fail due to surge and waves. Kennedy et al. (2011) performed a field reconnaissance survey after Hurricane Ike in 2008 to study the damages caused by the storm to coastal residential structures. The authors found that the critical factor to a building's survival was its elevation off of the ground. While there was a correlation between wave heights near the location of damaged structures, the height of the lowest horizontal member (LHM) was highly correlated to damages to the structure (Kennedy et al., 2011). Following the field study by Kennedy et al. (2011), Tomiczek et al. (2013) used the survey of damage to wood-frame coastal residential structures to develop fragility models considering multiple variables including wave height, buildings age, water velocity, and freeboard, which is a measurement of the distance from the crest of a wave to the LHM of a structure. Although the types of buildings surveyed differed slightly between the studies, the main conclusion drawn was that the freeboard of a structure is a significant variable affecting damage to the structure.

After Hurricane Sandy made landfall on the United States East Coast in 2012, multiple field surveys were conducted to evaluate the damages and failures of coastal structures on the New Jersey and New York shoreline. Hatzikyriakou et al. (2015) conducted both manual and laser scanning (LiDAR) based post-disaster surveys along the New Jersey shoreline to assess failure and damage types to coastal structures. The most common type of failure they found was separation from the foundation due to lateral and uplift forces. They also found that residential structures elevated on piles were much more likely to be less damaged (Hatzikyriakou et al. 2015). Tomiczek et al. (2017) also performed a field survey and developed a damage state classification system for the structures they surveyed. Once the structures could be classified, they were able to create a fragility model to predict damage states of residential structures based on a shielding parameter and other conditions such as wave crest height, water velocity, and freeboard (Tomiczek et al., 2017). In these post-disaster field surveys, the researchers found that many failed

159 residential structures were removed entirely from their foundations. Even wood-frame structures were
160 forced off their piles due to the strong lateral and uplift forces and insufficient connections to the piles.
161 These field surveys amplified the need to take an in-depth look at the damages and failure to residential
162 structures along the coast.

163 An early attempt to look at the failure of wood structures by waves using physical model testing
164 was made by Yeh et al. (1999), where they studied the behavior and response of breakaway walls. The tests
165 were conducted at full-scale in the Large Wave Flume at Oregon State University using lumber and
166 construction patterns used in practice. The researchers investigated the relationship between the connection
167 details used in the construction of breakaway walls and the wave forces that caused these connections to
168 fail (Yeh et al., 1999). Similar to the work of Yeh et al. (1999), Linton et al. (2013) studied subassembly
169 components of wooden walls at prototype scales subjected to solitary waves until failure using the same
170 wave flume but a different test apparatus. The researchers constructed three types of walls of various sizes
171 to study the performance of each wall type. Each wall was equipped with pressure sensors and load cells to
172 measure the wave forces from the tsunami-like solitary waves (Linton et al., 2013).

173 Wilson et al. (2009) conducted one of the first physical model experiments of an entire house using
174 a physical model study (see also Wilson (2008), Garcia et al. (2008), and van de Lindt et al. (2009)). They
175 constructed a 1:6 scale wood-frame residential structure and subjected it to tsunami-like solitary waves until
176 failure to study the effects of waves and surge on the structure. The researchers installed the specimen in
177 multiple ways: (1) with the front of the specimen normal to the wave direction and with the front of the
178 specimen parallel to the wave direction; (2) elevated on a plate about 10 cm above the ground and only
179 elevated 4 cm above the ground; and (3) with windows and doors closed and with windows and doors open
180 (Garcia, 2008; Lindt et al., 2009; Wilson, 2008). They found that the orientation and elevation of the
181 structure and the openings of the doors and windows had a significant effect on the loads the structure
182 experienced. They also found that waves breaking on or near the structure increased the measured forces.

183 In this study, the force and response of a scaled residential structure subjected to coastal hazards
184 are investigated, based on existing knowledge and previous works such as Wilson et al. (2008). For the

present study, both on-grade and elevated structures are considered, and several combinations of surge and wave conditions are considered to simulate Hurricane Sandy's conditions rather than solitary waves to simulate tsunamis, which can be found in previous research. Moreover, the complexity of the instrumentation is increased relative to previous works to provide a better understanding of the structural response and progressive damage of the structures prior to failure.

3. Experimental Design and Setup

Similar to the way that the experimental designs of Bradner et al. (2011) and Park et al. (2017) were informed by the failure of bridges during Hurricane Katrina and residential structures during Hurricane Ike, respectively, this experiment was designed based on the damages observed to residential structures following Hurricane Sandy. Section 3.1 provides some background on the observed coastal conditions. Section 3.2 describes the experimental design, including an overview of the Directional Wave Basin, and Section 3.3 summarizes the design and construction of the specimens completed earlier (Burke, 2018; Karny, 2018), and Section 3.4 provides the detail of the instrumentation installed on the specimen.

3.1. Coastal conditions

Hurricane Sandy made landfall on the East Coast of the United States in 2012, causing extensive damage along the coast of New Jersey (Blake et al., 2013; Hatzikyriakou et al., 2015; Tomiczek et al., 2017). Field surveys conducted by Hatzikyriakou et al. (2015) and Tomiczek et al. (2017) identified Ortley Beach, New Jersey, as one of the areas with the most significant damage due to storm surge and waves. A United States Geological Survey (USGS) tide gauge located in Ortley Beach measured a storm tide of 2.65 m above the North American Vertical Datum 88, which corresponds to an estimated inundation level of 0.85 m in the Ortley Beach area (Blake et al., 2013). Tide gauges in other areas of New Jersey recorded inundation depths of 2.74 m above the local ground elevation (Blake et al., 2013). Hatzikyriakou et al. (2015) and Tomiczek et al. (2017) surveyed 372 residential structures and 380 residential structures in Ortley Beach following Hurricane Sandy, respectively. Hatzikyriakou et al. (2015) and Tomiczek et al.

(2017) recorded the failure modes of the structures and the severity of damage. Figure 1 shows example damages to these structures by the combination of surge and waves (Tomiczek et al., 2017).

Figure 1. Damaged residential structures in Ortley Beach, New Jersey, after Hurricane Sandy in 2012. Photo courtesy: T. Tomiczek.

3.2. Experimental design

The Directional Wave Basin (DWB) at Oregon State University was used to create an idealized section of coastline to test the impact of waves on residential structures. Figure 2 shows the profile and plan view of the experiment in the Directional Wave Basin. The basin was 48.8 m long, 26.5 m wide, and 2.13 m deep with a multi-directional piston-type wavemaker. The test section for this experiment started 9.75 m from the wavemaker and was 10 m wide and consisted of a 20 m, 1:20 sloped section that approximated the alongshore uniform bathymetry of the New Jersey shoreline near Ortley Beach. The sloped section led to a 10 m long flat section elevated 1.0 m above the floor of the basin to represent the flat barrier island where Ortley Beach is located. The two specimens were located on the flat section of the testbed 3.5 m from the shore break. At 1:6 scale, this corresponds to 21 m (69 ft) from the shoreline. Sand dunes and other coastal features were not included.

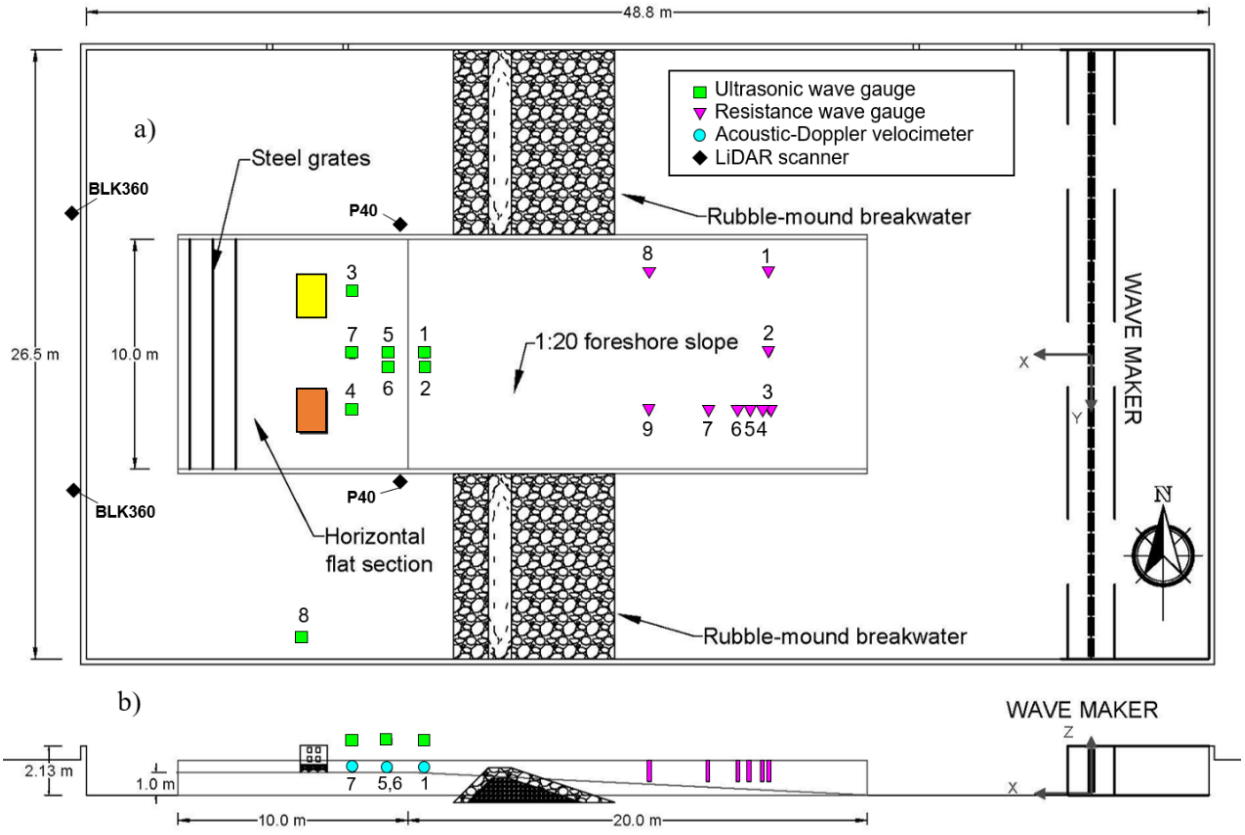

Figure 2. Sketch of directional wave basin. Plan view (a) and profile view (b).

Figure 2 also shows some of the instrumentation used in this experiment, including nine wire resistive wave gauges (wg1-wg9) located offshore, seven ultrasonic wave gauges located onshore near the specimens (uswg1-uswg7), four acoustic-Doppler velocimeters (adv1, adv5, adv6, and adv7), and the locations of the onshore LiDAR scanner (Leica Geosystems BLK360 Scanner) and the offshore LiDAR scanner (Leica Geosystems P40 Scanner). Scanners provided millimeter precision of specimen locations. One ultrasonic wave gauge (uswg8) was installed outside of the test section for a previous experiment. Table 1 lists the x, y, and z coordinates of each instrument where $x = 0$ m, $y = 0$ m, and $z = 0$ m is the position of the center of the wavemaker on the base of the basin. In this study, the x-direction is the cross-shore direction, and the y-direction is the long-shore direction. The ultrasonic wave gauges and resistive wave gauges recorded data with a sampling rate of 100 Hz, and the sampling rate for the ADVs was also 100 Hz.

240 Table 1. Instruments and their locations used to measure hydrodynamic conditions.

Instrument	data column	*x* (m)	*y* (m)	*z* (m)
Ultrasonic Wave Gauge	uswg1	29.00	0.02	2.29
Ultrasonic Wave Gauge	uswg2	28.99	0.50	2.30
Ultrasonic Wave Gauge	uswg3	32.18	-2.38	2.34
Ultrasonic Wave Gauge	uswg4	32.24	2.47	2.34
Ultrasonic Wave Gauge	uswg5	30.59	0.00	2.36
Ultrasonic Wave Gauge	uswg6	30.58	0.52	2.43
Ultrasonic Wave Gauge	uswg7	32.17	0.04	2.38
Ultrasonic Wave Gauge	uswg8	34.35	12.38	1.84
Resistive Wave Gauge	wg1	14.05	-3.54	n/a
Resistive Wave Gauge	wg2	14.05	-0.06	n/a
Resistive Wave Gauge	wg3	14.04	2.47	n/a
Resistive Wave Gauge	wg4	14.34	2.48	n/a
Resistive Wave Gauge	wg5	14.90	2.48	n/a
Resistive Wave Gauge	wg6	15.39	2.47	n/a
Resistive Wave Gauge	wg7	16.69	2.47	n/a
Resistive Wave Gauge	wg8	19.28	-3.54	n/a
Resistive Wave Gauge	wg9	19.25	2.49	n/a
Acoustic Doppler Velocimeter	adv1	29.02	-0.02	1.02
Acoustic Doppler Velocimeter	adv5	30.59	0.00	1.01
Acoustic Doppler Velocimeter	adv6	30.58	0.48	1.01
Acoustic Doppler Velocimeter	adv7	32.16	-0.12	1.02

241

242 Figure 3 is a photo of the experimental setup after Trial 3. Three steel grates were installed one
243 meter apart on the onshore side of the specimens on the westernmost part of the flat section to minimize
244 reflection. Rubble-mound breakwaters were constructed on both sides of the test section to dissipate waves.
245 Figure 3 also shows the on-grade specimen in yellow and the elevated specimen in orange described in
246 detail in the next sections. The distance between the two specimens was 3.2 m.

Figure 3. Photo of the directional wave basin after Trial 3. On-grade specimen (left) shows damage from previous trials.

3.3. Specimen construction

The two specimens tested in this experiment were based on the design and construction detailed in the previous work of Burke (2018) and Karny (2018). This subsection provides an overview of the specimen design discussed in Burke (2018) to provide context for the experimental model setup and testing. Burke (2018) designed the specimens to model typical residential structures in Ortley Beach, New Jersey. Google Street View was used to characterize the buildings and Burke (2018) found that many residences were rectangular and had a front to side ratio of approximately 3:2. Although these structures were newly constructed after the disaster, they were deemed to be representative of structures in that area prior to the storm.

Burke (2018) chose a length scale of 1:6 consistent with Wilson et al. (2008) due to the 3.6 m (12 ft) width of the Large Wave Flume at Oregon State University where the initial tests were planned. The specimens were constructed to be 1.23 m by 1.83 m (4 ft by 6 ft), which is equivalent to a 7.32 m by 11 m (24 ft by 36 ft) prototype specimen. While a length scale was defined to be 1:6, structural stiffness and

capacity do not scale the same way and proportionally since they depend on factors such as the size of nails, local models of damage and failure of nails, and their spacing. In addition, when working with timber shear walls, the sheathing is also of extreme importance and the modes of deformation and failure can include a combination of shear and bending of the wall and therefore provide for a complex scaling problem. Burke (2018) originally constructed eight scaled wall panels that varied in nail spacing and shear wall size to determine the spacing to be used. The walls were constructed using Douglas fir wood as the wall studs and Luan plywood was used for the wall sheathing. The nail spacing on these test walls varied from 2.54 cm to 20.3 cm (30.5 cm to 122 cm [6 in to 48 in] prototype) and the shear wall size varied between 20.3 cm by 40.6 cm and 40.6 cm by 40.6 cm (1.23 m by 2.66 m and 2.44 m by 2.44 m [4 ft by 8 ft and 8 ft by 8 ft] prototype). Burke (2018) performed monotonic pushover tests on the various test walls and found that the test walls with a scaled nail spacing of 5.1 cm (2 in) and a shear wall size of 40.6 cm by 40.6 cm (16 in by 16 in) had structural stiffness values most similar to full-scale 2.44 m by 2.44 m (8 ft by 8 ft) wood walls. Thus, additional monotonic pushover, in-plane shear wall tests were performed on 13 identical 40.6 cm by 40.6 cm 1:6 scaled wall panels (2.44 m by 2.44 m [8 ft by 8 ft] prototype) with 5.1 cm (2 in) nail spacing. Burke (2018) then compared the structural stiffness and strength obtained from the testing of the scaled specimens to the experimental data available in the literature (e.g., Wilson et al. 2008; Koliou et al. 2018).

The goal of the pushover tests was to determine the stiffness and strength of the walls. Force-displacement curves were generated from the pushover test data for each wall, which in the interest of brevity of this paper are not included but can be found in Burke (2018). The stiffness is found by calculating the slope of the linear elastic region, which was taken approximately between 10% and 40% of the peak load. Based on the average stiffness value, the per unit length stiffness was determined. The per unit length stiffness was important to allow for transferring the results from the tested walls (2.44 m by 2.44 m [8 ft by 8 ft]) to the constructed specimen walls (7.32 m by 2.44 m [24 ft by 8 ft] and 11.0 m by 2.44 m [36 ft by 8 ft]). The per unit length stiffness also makes it easier for a direct comparison to standard values at full-scale (see Burke 2018 for details). At the 1:6 scale used to construct the specimen, the stiffness per unit length of wall was determined to be 351 N/mm per m of wall length (51 lbs/in/in).

When brought to full-scale this value equates to 2065 N/mm per m of wall length (300 lbs/in/in or 3.7 kips/in/ft), which is approximately 3 times the standard value for a 1.22 m by 2.44 m (4 ft by 8 ft) wood wall structural panel (Applied Technology Council, 2017). Burke (2018) also performed pushover tests on the fully constructed specimens and scaled the stiffness results up by a factor of six. When connecting the walls on the fully constructed specimens, the nail spacing was not maintained between each wall panel and between each floor. The stiffness of the specimen walls decreased significantly after constructing the entire specimen and the stiffness was only 6.5% larger than the standard stiffness of the full-scale 1.22 m by 2.44 m (4 ft by 8 ft) wood walls. Burke (2018) stated that the decrease in stiffness from the individual test wall pushover tests is most likely due to the window and door openings in the walls.

Burke (2018) also found that many coastal residences in the Ortley Beach, NJ, area were elevated with a crawl space of about 1.23 m (4 ft). Hatzikyriakou et al. (2015) and Tomiczek et al. (2017) found that the residential structures on the Bolivar Peninsula, TX, were elevated on piles had a higher survival rate than homes that were not on piles. To accommodate these regional differences in construction elevations, Burke (2018) constructed one of the specimens to be on-grade and one of the specimens to be on piles to study the effects of elevation. Burke (2018) referred to the Coastal Construction Manual (CCM, FEMA, 2011) to construct the elevated specimen. Design examples in the CCM used pile dimensions of 30.5 cm by 30.5 cm (12 in by 12 in), which was used in the construction of the elevated specimen. Girders were also constructed so the piles could connect to the superstructure of the specimen following the CCM. The girders were two timber members nailed together that were connected to the top of each pile where the piles were "notched" for the girder-to-pile connection. The elevated specimen was also constructed with 5.08 cm by 25.4 cm (2 in by 10 in) floor joists on the bottom side of the specimen oriented in the *x*-direction to follow the IRC requirements. It is noted that the floor itself was not modeled for this study and was composed of a single sheet of plywood, 1.91 cm (0.75 in) thick. A single plywood sheet 1.91 cm (0.75 in) thick was also used as the roof for both of the specimens in this study.

315 Two main modifications of the elevated specimen designed by Burke (2018) were made in this
316 study. The first modification was to shorten the piles so that the bottom elevation of the LHM of the elevated
317 specimen was 35 cm above the test section corresponding to 2.1 m (6.9 ft). This is slightly lower than the
318 3.0 to 3.7 m (10 to 12 ft) elevation more commonly associated with elevated residential structures and was
319 necessitated by the physical limitations of the DWB at that time. Nevertheless, the 35 cm (2.1 m prototype)
320 elevation was sufficient to have a significantly different response than the on-grade specimen.

321 The second modification was the construction of the cross-bracing on the piles in the *x*-direction as
322 prescribed in the CCM. A drawing of each specimen can be seen in Figure 4 with the modifications that
323 were done. The on-grade specimen had to be raised 9.7 cm for the load cells to be correctly installed
324 underneath it but is still considered to be "on-grade" for this study. Additional specimen information, such
325 as window and door dimensions, can be found in Duncan et al. (2020).

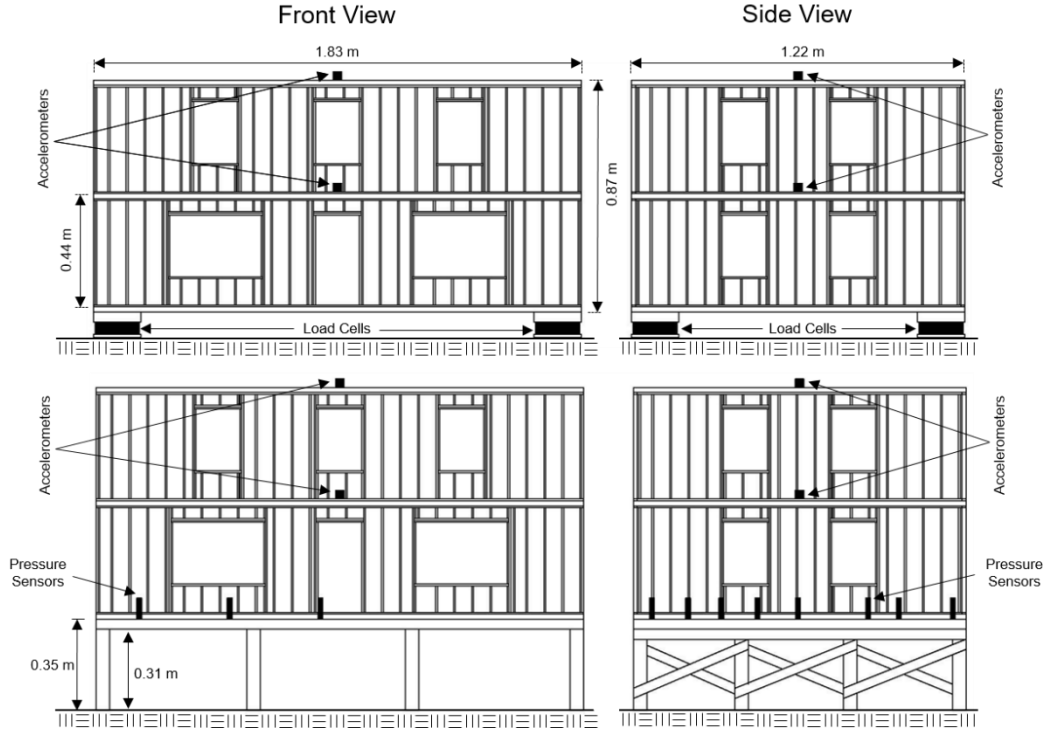

326

327 Figure 4. Front view and side view of the on-grade specimen (top) and elevated specimen (bottom).

328

3.4. Specimen instrumentation

Table 2 lists the instruments installed within and around the specimens, including 12 pressure sensors (press1-press12), four load cells (load1-load4), four accelerometers (accel1-accel4), and three string potentiometers (sp1-sp3). Figure 5 shows the configuration of the four vertical load cells the on-grade specimen was installed on and the configuration of the 12 pressure gauges installed in the elevated specimen. The gauges were installed along the bottom of the elevated specimen to determine the uplift pressures. Eight of the sensors (press1, press4-press10) were installed along the center of the specimen to measure the uplift pressure distribution in the *x*-direction. These sensors were installed 7.6 cm from the centerline of the specimen in the *y*-direction due to floor joists. The remaining four sensors (press2, press3, press11, and press12) were installed along the front and back of the bottom of the specimen to evaluate the variation in pressure in the *y*-direction. The pressure sensors are GE-DRUCK PDCR830 gauges and have a combined linearity and hysteresis of 0.1%. The on-grade specimen was equipped with two accelerometers, accel1 on the second level and accel2 on the top level of the specimen, which measured the acceleration of the specimens in the *x*, *y*, and *z* direction. The elevated specimen was also equipped with two accelerometers, accel3 on the second level of the specimen and accel4 on the top of the specimen. The accelerometers on both specimens used during the wave loading testing were of the PCB model W356A12 type. The sensitivity of the accelerometers as provided by the manufacturer were confirmed through testing performed on a shaker at Oregon State University. Figure 4 shows the location of these accelerometers. The pressure sensors, load cells, and accelerometers recorded data with a sampling rate of 1,000 Hz. The structural tests used additional instruments, including the string potentiometers listed in Table 2 that were removed once the structural tests were complete. The string potentiometers are UniMeasure HX-PB-40 with a linearity of 0.1% full scale.

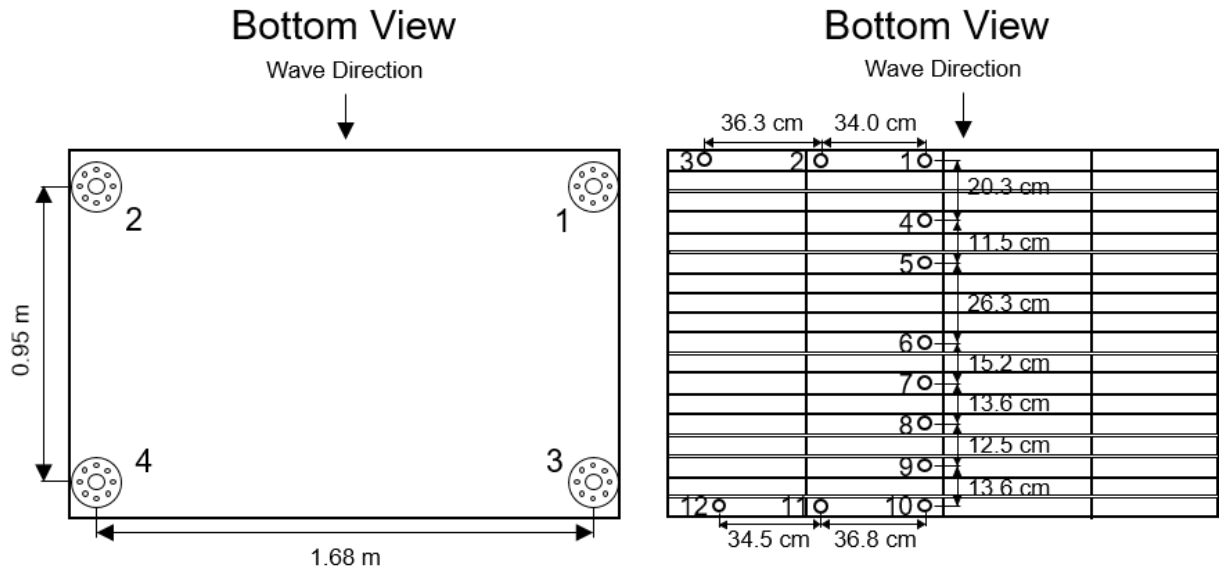

Figure 5. Drawing of the load cell configuration underneath the on-grade specimen (left) and the pressure sensor configuration on the bottom of the elevated specimen (right).

Table 2. Instruments and their locations used to measure the pressure, force, and response of the specimens.

Instrument	Data Column	*x* (m)	*y* (m)	*z* (m)	Used in Hydrodynamic Test	Used in Structural Tests
Pressure Sensor	press1	33.30	2.59	1.35	Y	
Pressure Sensor	press2	33.29	2.93	1.35	Y	
Pressure Sensor	press3	33.30	3.29	1.35	Y	
Pressure Sensor	press4	33.50	2.59	1.35	Y	
Pressure Sensor	press5	33.61	2.59	1.35	Y	
Pressure Sensor	press6	33.88	2.58	1.35	Y	
Pressure Sensor	press7	34.03	2.59	1.35	Y	
Pressure Sensor	press8	34.17	2.59	1.35	Y	
Pressure Sensor	press9	34.29	2.58	1.35	Y	
Pressure Sensor	press10	34.43	2.58	1.35	Y	
Pressure Sensor	press11	34.42	2.95	1.35	Y	
Pressure Sensor	press12	34.44	3.29	1.35	Y	
Load Cell (vertical)	load1	33.40	-3.36	1.05	Y	
Load Cell (vertical)	load2	33.40	-1.68	1.05	Y	
Load Cell (vertical)	load3	34.35	-3.36	1.05	Y	
Load Cell (vertical)	load4	34.35	-1.68	1.05	Y	
Load Cell (horizontal)	load5	n/a	n/a	n/a		Y
Accelerometer (*x*-direction)	accel1*x*	33.87	-2.52	1.56	Y	Y

Accelerometer (*y*-direction)	accel1*y*	33.87	-2.52	1.56	Y	Y
Accelerometer (*z*-direction)	accel1*z*	33.87	-2.52	1.56	Y	Y
Accelerometer (*x*-direction)	accel2*x*	33.87	-2.53	1.98	Y	Y
Accelerometer (*y*-direction)	accel2*y*	33.87	-2.53	1.98	Y	Y
Accelerometer (*z*-direction)	accel2*z*	33.87	-2.53	1.98	Y	Y
Accelerometer (*x*-direction)	accel3*x*	33.86	2.50	1.79	Y	Y
Accelerometer (*y*-direction)	accel3*y*	33.86	2.50	1.79	Y	Y
Accelerometer (*z*-direction)	accel3*z*	33.86	2.50	1.79	Y	Y
Accelerometer (*x*-direction)	accel4*x*	33.86	2.50	2.22	Y	Y
Accelerometer (*y*-direction)	accel4*y*	33.86	2.50	2.22	Y	Y
Accelerometer (*z*-direction)	accel4*z*	33.86	2.50	2.22	Y	Y
String Potentiometer	sp1	34.48	2.54	1.36		Y
String Potentiometer	sp2	34.48	2.53	1.78		Y
String Potentiometer	sp3	34.48	2.53	2.20		Y

4. Methods for Structural Property Characterization

In-situ tests were performed on each specimen in both the *x*-direction and *y*-direction before the hydrodynamic testing to determine the structural properties of the specimens, which were lateral load "pull" tests and free vibration tests. In addition, the recorded accelerations were used to determine the fundamental frequencies of the structure during the surge and wave trials. Section 4.1 provides details of the methods used for the in-air structural tests and Section 4.2 includes the methods for determining the in-water structural properties.

4.1. In-air specimen lateral force and free vibration tests

The purpose of the lateral force and free vibration tests were to determine the stiffness, damping ratio, and natural frequency of the specimens. These were done sequentially for both specimens as described in this subsection. In the lateral force testing, a lateral force was applied at the top level of the specimens, and the displacements were measured at different elevations simultaneously using string potentiometers. A crane pulled the specimens through a pulley and lever system attached to the top edge of the specimens with a guy-wire. The force was measured with an in-line load cell (load5 in Table 2). String potentiometers were used to measure the displacement of the specimens in the direction of the applied force, which were connected to the outside of the specimens. These were all connected to a rigid beam fixed floor of the wave

basin. The displacements were measured at the second level and the top level of the on-grade specimen. The displacements were measured at the first, second, and top level when performing the lateral load tests on the elevated specimen. In the lateral force testing, the forces were incrementally increased to force of approximately 0.30 kN as measured on a load cell installed on the crane.

Once the peak force was reached, the guy-wire was cut, thus creating a pluck-type test and allowing the specimen to vibrate freely until it came to rest. The accelerometers installed on the structures were used to measure the specimen responses in the *x*, *y*, and *z* directions. These tests were repeated five times in both the *x*-direction and *y*-direction for each specimen.

The instruments for each trial of the lateral load and free vibration tests consisted of a load cell (load5 in Table 2) to measure the force that was applied to the specimens and two accelerometers installed at the floor levels of the specimen. The accelerometers were the same instruments described in Section 3.3.

The structural stiffness of the specimens is a measurement of their ability to resist deformation when a load is applied. The load applied to the specimens during the lateral force tests was plotted against the displacement from the point the load was applied to determine the slope with provided the stiffness of the specimen.

The natural frequency was found using the free vibration tests, ambient vibration tests and the forced vibration tests. A power spectral density was computed of the accelerations measured on the top level of each specimen during the free vibration test, and the peak frequency was identified as the specimen's natural frequency.

The damping ratio was found from the oscillations of the accelerometers on the top levels of the specimens measured using

$$\zeta = \frac{1}{2\pi j} \ln \left(\frac{u_i}{u_{i+j}}\right) \quad (1)$$

from Chopra (1995), where u_i is the acceleration at one chosen peak after the cut, j is the number of cycles away a second chosen peak is after the oscillations have damped, and u_{i+j} is the acceleration at the second peak j cycles away from u_i.

Based on the lateral force testing, Table 3 lists the stiffness of each specimen in the *x*-direction and *y*-direction. The mean stiffness of the on-grade specimen was 577 N/mm and 451 N/mm in the *x*-direction and *y*-direction, respectively. The mean stiffness of the elevated specimen was 266 N/mm and 406 N/mm in the *x*-direction and *y*-direction, respectively.

Table 3 lists the natural frequency for each specimen in the *x*- and *y*-direction from the free vibration tests. The mean natural frequencies of the on-grade specimen derived from the free vibration tests were 28.3 Hz and 28.2 Hz in the *x*-direction and *y*-direction, respectively. The mean natural frequencies of the elevated specimen derived from the free vibration tests were 21.0 Hz and 15.2 Hz in the *x*-direction and *y*-direction, respectively. Table 3 lists the damping ratio for each specimen in the *x*- and *y*-directions. The mean damping ratio of the on-grade specimen was 6.1 % and 7.2 % in the *x*-direction and *y*-direction, respectively. The mean damping ratio of the elevated specimen was 6.6 % and 3.8 % in the *x*-direction and *y*-direction, respectively.

Table 3. Structural properties of the on-grade specimen and elevated specimen. The table is in the format x (y, z) where x is the mean value from the five trials, y is the standard deviation, and z is the standard error.

	On-grade Specimen		Elevated Specimen	
Structural Property	x-direction	y-direction	x-direction	y-direction
Stiffness (N/mm)	577 (77.8, 34.8)	451 (49.0, 21.9)	266 (19.7, 8.8)	406 (54.1, 24.2)
Damping ratio (%)	6.1 (0.73, 0.33)	7.2 (1.50, 0.66)	6.6 (0.61, 0.27)	3.8 (0.40, 0.18)
Natural freq. (Hz)	28.3 (0.24, 0.11)	28.2 (0.56, 0.25)	21.0 (0.41,0.18)	15.2 (0.13,0.06)

4.2. In-water specimen structural properties for damage identification

The specimens were subjected to hydrodynamic testing, as described in the Section 5. Using the recorded acceleration data discretized in intervals of 0.001s, and grouping the acceleration signals for each trial into groups of four to twelve waves, the natural frequencies were estimated through peak picking from the power spectral density functions obtained using the *pspectrum* function in MATLAB and a frequency resolution of 0.5. Naturally, due to the short duration of each wave (~20 seconds) the uncertainty in the results is captured through the grouping of the wave data.

5. Hydrodynamic Testing

For specimen tests discussed previously (e.g., Bradner et al., 2011; Park et al., 2017), it is possible to use a wide range of testing conditions such as regular waves, irregular waves, and solitary (tsunami-like) waves and can vary the water depth, wave height, and wave period. For destructive tests mentioned before (e.g., Linton et al., 2013; Wilson et al., 2008; Yeh et al., 1999), a narrower range of conditions are used, and previous researchers from these tests had generally used either solitary (tsunami-like) or regular waves. For the experiments presented here, the hydrodynamic tests focused on regular waves with one predominant wave period of T = 4.5 s (11 s prototype), with the exception of Trials 9 and 10, which had a wave period of T = 3.5 s and T = 5.5 s, respectively. Regular waves were used in this study for simplicity and to easily identify the wave conditions that caused the specimens to fail. They were also used to be consistent with previous studies (e.g., Bradner et al., 2011; Park et al., 2017). Table 4 shows the hydrodynamic conditions for the 21 trials of the experiment. The water depth at the wavemaker, h_0, ranged from 1.10 m to 1.45 m. The test section was elevated 1.0 m above the basin floor, so the corresponding water depth at the specimen, h, ranged from 0.10 m to 0.45 m, which corresponds to a range from 0.6 m (2.0 ft) to 2.7 m (8.9 ft) prototype, similar to the observed surge conditions at Ortley Beach during Hurricane Sandy (Blake et al., 2013). Column 3 lists the air gap of the elevated specimen, a, defined as the elevation of the bottom of the LHM of the elevated specimen relative to the still water level. When the mean water level is above the LHM, the air gap is negative. The elevation of the LHM of the elevated structure was 35 cm (2.1 m prototype), and the elevation of the LHM of the on-grade structure was 9.7 cm (0.58 m prototype).

The regular waves used for this experiment were characterized by the nominal input wave height at the wavemaker, H_{in} and wave period, T. The input wave heights ranged from 0.1 to 0.4 m, which corresponded to a range of 0.6 m (2.0 ft) < H_{in} < 2.4 m (7.8 ft) in prototype, similar to large storm waves produced by hurricanes. It is noted that the wave heights at the specimens were often lower than the input wave height due to depth limited breaking and were occasionally larger than the input wave height due to shoaling on the 1:20 slope before reaching the specimen.

Table 4. Water levels, input wave conditions, breaking type, number of cumulative waves impacting the specimens (N_W), and scans conducted for all trials.

Trial	h_0 (m)	h *(m)*	a (m)	H_{in} (m)	T (s)	Breaking Type at Specimens	N_{WO}	N_{WE}	Notes
1	1.10	0.10	0.25	0.1	4.5	Broken	40	-	Scan before Trial 1
2	1.10	0.10	0.25	0.4	4.5	Broken	81	-	Scan after Trial 2
3	1.12	0.12	0.23	0.1	4.5	Breaking	122	-	
4	1.20	0.20	0.15	0.2	4.5	Broken	164	-	
5	1.20	0.20	0.15	0.3	4.5	Broken	206	-	Scan after Trial 5
6	1.30	0.30	0.05	0.1	4.5	Nonbreaking	246	40	
7	1.30	0.30	0.05	0.2	4.5	Breaking	286	80	
8	1.30	0.30	0.05	0.3	4.5	Broken	327	121	
9	1.30	0.30	0.05	0.3	3.5	Broken	380	174	
10	1.30	0.30	0.05	0.3	5.5	Broken	414	208	Scan after Trial 10
11	1.35	0.35	0.00	0.1	4.5	Nonbreaking	454	248	
12	1.35	0.35	0.00	0.2	4.5	Breaking	461	289	On-grade specimen fails
13	1.35	0.35	0.00	0.3	4.5	Broken	-	330	
14	1.35	0.35	0.00	0.4	4.5	Broken	-	371	Scan after Trial 14
15	1.40	0.40	-0.05	0.1	4.5	Nonbreaking	-	412	
16	1.40	0.40	-0.05	0.2	4.5	Breaking	-	453	
17	1.40	0.40	-0.05	0.3	4.5	Breaking	-	494	
18	1.40	0.40	-0.05	0.4	4.5	Broken	-	535	Scan after Trial 18
19	1.45	0.45	-0.10	0.1	4.5	Nonbreaking	-	576	
20	1.45	0.45	-0.10	0.2	4.5	Breaking	-	617	
21	1.45	0.45	-0.10	0.3	4.5	Breaking	-	620	Elevated specimen fails

Approximately 40 regular waves were generated, which lasted about 3 minutes for each trial. The type of waves observed at the specimen were broken, breaking, or nonbreaking wave. The cumulative number of waves that interacted with the specimen was recorded for both the on-grade specimen, N_{WO}, and the elevated specimen, N_{WE}. The on-grade specimen failed during Trial 12, and the elevated specimen failed during Trial 21. After Trial 21, the foundations were removed from the wave basin, and Trial 1 to Trial 21 were repeated to measure the hydrodynamic conditions without the effects of the specimens.

Before each increase in water level, LiDAR scans were taken of the wave basin to qualitatively and quantitatively track the progressive damage of each specimen. A Leica Geosystems P40 Scanner and a BLK360 Scanner were used from multiple angles on the onshore and offshore sides of the specimens. Each scan took approximately 15 minutes with the scanners in different positions. The positions of the scanners can be seen in Figure 2. Methods presented in Barbosa et al. (2017) and Wood et al. (2017) were used to quantify the damage.

462 **5.1. Time series data**

463 The hydrodynamic testing had a variety of water levels, wave heights, and breaking types ranging
464 from nonbreaking waves to waves breaking directly against the specimens. Figure 6 shows an example of
465 the water level time series from wg1, uswg3, and uswg4 and water velocity time series in the *x*-direction
466 from adv7 from Trial 7 and Trial 18. Based on the video recordings and trial notes from Table 4, the waves
467 during Trial 7 were breaking directly in front of the specimens, and the waves during Trial 18 were breaking
468 several meters offshore from the specimens.

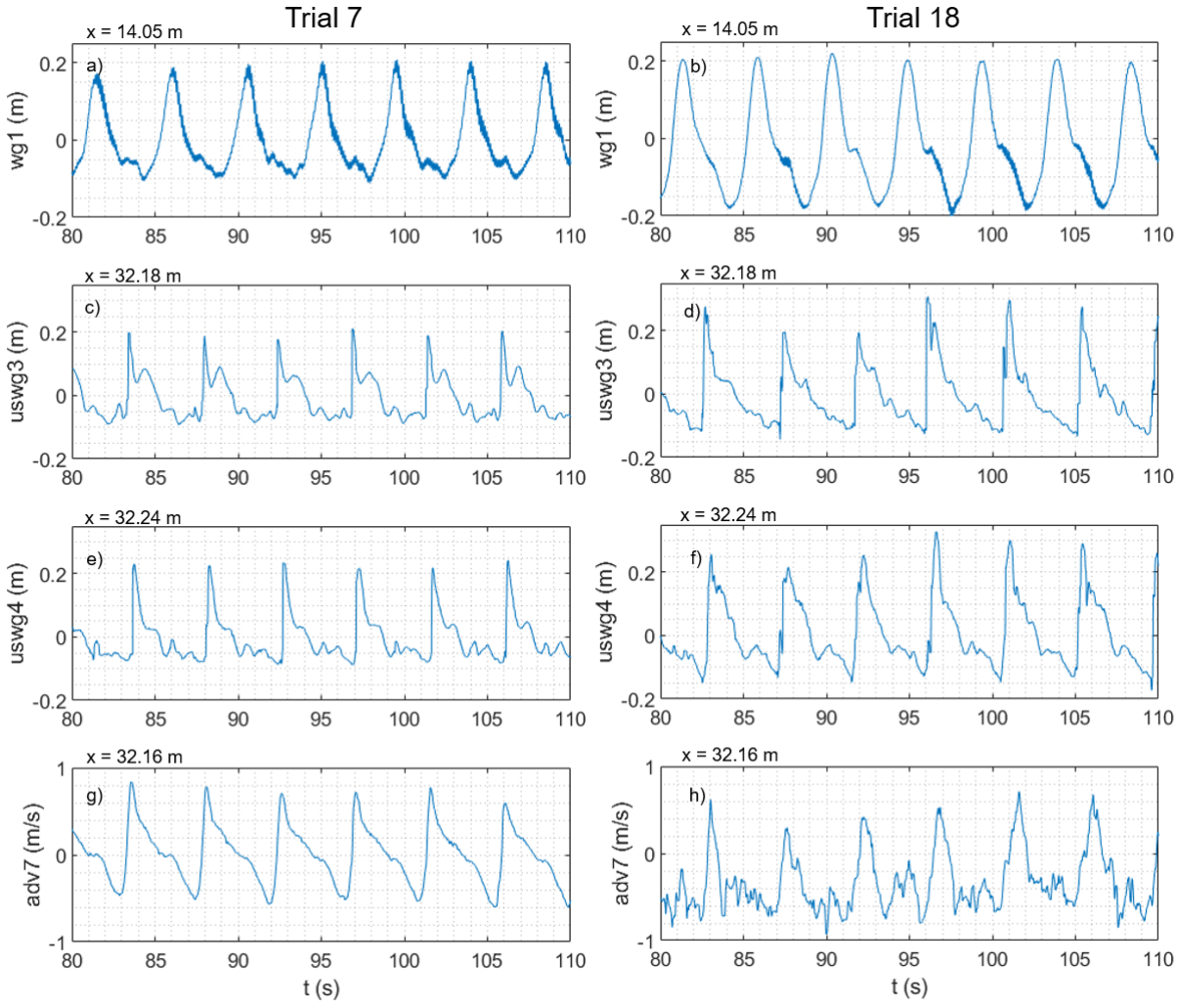

469

470 Figure 6. Time series of the hydrodynamic conditions from Trial 7 (left, h_0 = 1.30 m) and Trial 18 (right,
471 h_0 = 1.40 m). Panels a-f show free surface elevations and g-h show wave-induced water velocities in the *x*-
472 direction. The *x*-position of each sensor is also indicated above each panel.

473

Trial 7 had a water depth of 1.30 m at the wavemaker, which relates to a 0.30 m water depth at the specimens and an air gap of 0.05 m relative to the elevated specimen. Trial 18 had a water depth of 1.40 m at the wavemaker, which relates to a 0.45 m water depth at the specimens and an air gap of -0.05 m relative to the elevated specimen. The waves breaking directly on the specimens during Trial 7 and the negative air gap during Trial 18 led to relatively large forces measured by the load cells underneath the on-grade specimen and large uplift pressures on the elevated specimen. Figure 7 shows the overturning force measured by the load cells underneath the on-grade specimen (Figure 7a, c, e, and g), uplift pressures on the bottom of the elevated specimen (Figure 7b, d, f, h), and accelerations on the top level of both specimens (Figure 7i, j). Figure 7a, c and Figure 7e, g show that the front and back pairs of load cells are uniform as would be expected for the normally incident waves. The loads shown here are consistent with Wilson et al. (2008), Garcia et al. (2008), and van de Lindt et al. (2009). In Figure 7b, d, f, and h, an apparent decrease in uplift pressure can be seen as waves propagate from the front of the specimen to the back. Figure 7i, j show that there are large accelerations that occur with the initial impact by the wave on the structure and that these accelerations dampen before the arrival of the subsequent wave.

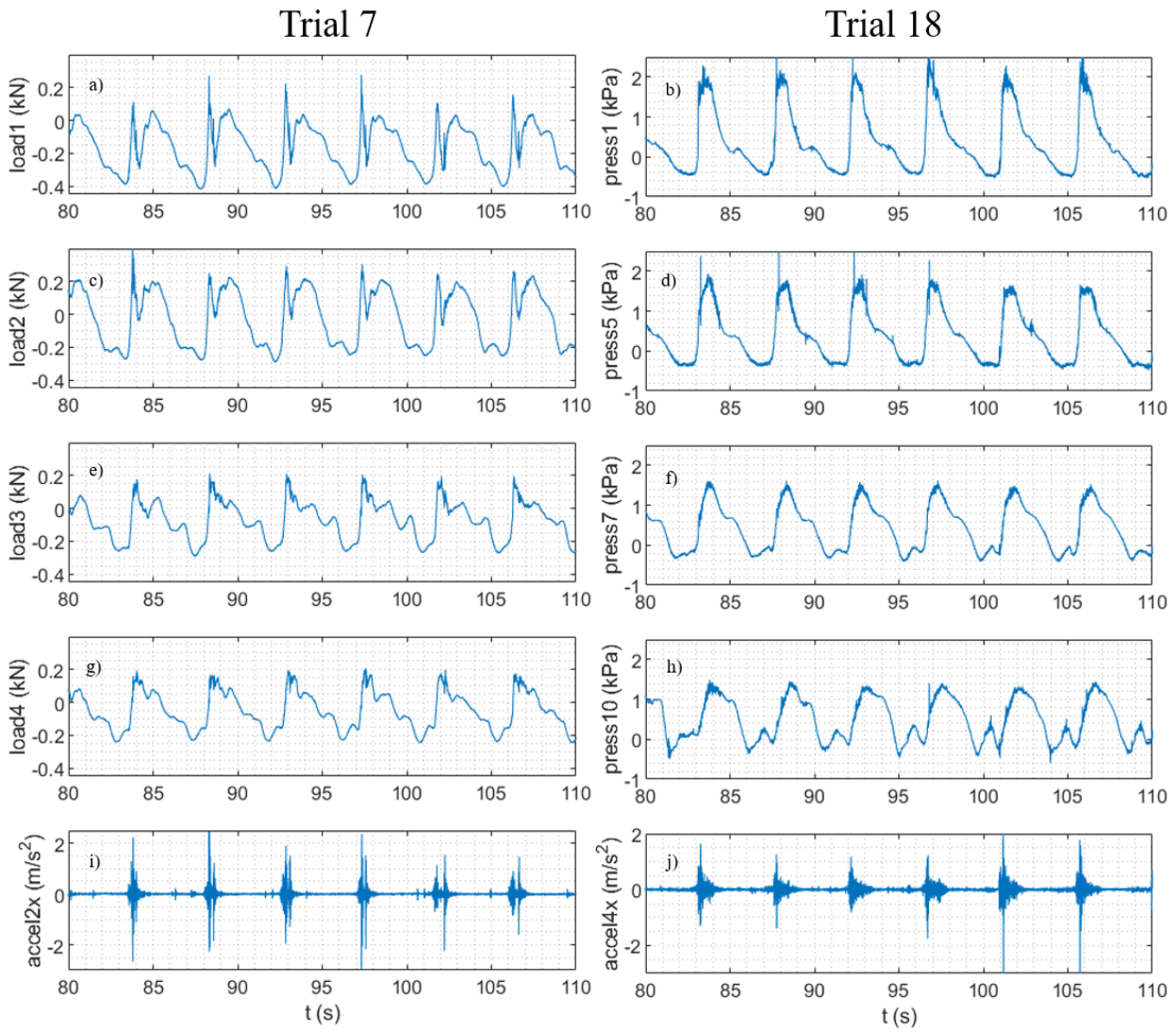

Figure 7. Time series of load cells 1-4 and accelerometer 2 on the on-grade specimen from Trial 7 (left, h_0 = 1.30 m). Time series of pressure sensors 1, 5, 7, and 10 and accelerometer 4 on the elevated specimen from Trial 18 (right, h_0 = 1.40 m). Both accelerometer time series (i and j) are in the x-direction.

5.2. Ensemble averaging and wave classification

In general, Figures 9 and 10 show that the wave forcing and structural response are repeatable patterns with each wave period. Subsequently, ensemble averaging is used to find representative parameters for each trial, such as wave heights, pressures, and loads. The ensemble average is performed in the time domain by the identification of waves by zero-crossing analysis. About 35 waves were averaged for each trial and wave ramp up and ramp down were not included in the ensemble averaging. Figure 8 shows

examples of ensemble-averaged free surface elevations of Trial 7, Trial 18, and Trial 19, where t = 0 s is the beginning of a wave period. Trials 7, 18, and 19 are examples of breaking, broken, and nonbreaking waves, respectively. Each plot also shows one standard deviation above and below the ensemble-averaged water surface elevations. The free surface elevations were taken from uswg3, uswg7, and uswg4, which were the wave gauges directly in front of the on-grade specimen, in the middle of the specimens, and in front of the elevated specimen, respectively. These ensemble-averaged water surface elevations are used to characterize the wave height at the specimens for each trial. Table 5 lists the ensemble-averaged wave heights, $\overline{H}$, offshore using wg1 and wg2 as well as wave heights measured in front of each specimen using uswg3, uswg7, and uswg4. It is noted that certain wave heights are not included in the table due to insufficient wave gauge readings from waves overtopping resistive wave gauges or water splashing on the face of ultrasonic wave gauges and interfering with their measurements.

A wave reflection analysis was completed using the nine resistive wave gauges (wg1-wg9) located offshore from the specimens according to the recommendations from Mansard and Funke (1980). The wave reflection analysis was intended to identify the far field average reflection from the test section, as well as to detect the formation of cross-waves, particularly during the experiments of overland flow. Wave reflection coefficients ranging from 10% to 45% have been obtained, and the contribution of the specimens increased the reflected wave energy by 10% to 25%. The finite width of the structures, and the varying geometry as the residences sustained more damage and overtopping, significantly increased the scattering of the results, preventing the generalization of a response model relating the wave energy reflection and the progressive damage to the specimens. The incident waves were also subject to significant transformation (shoaling and breaking) before impacting the specimens. Hence, it was determined more realistic to consider the wave heights near the toe of the specimens.

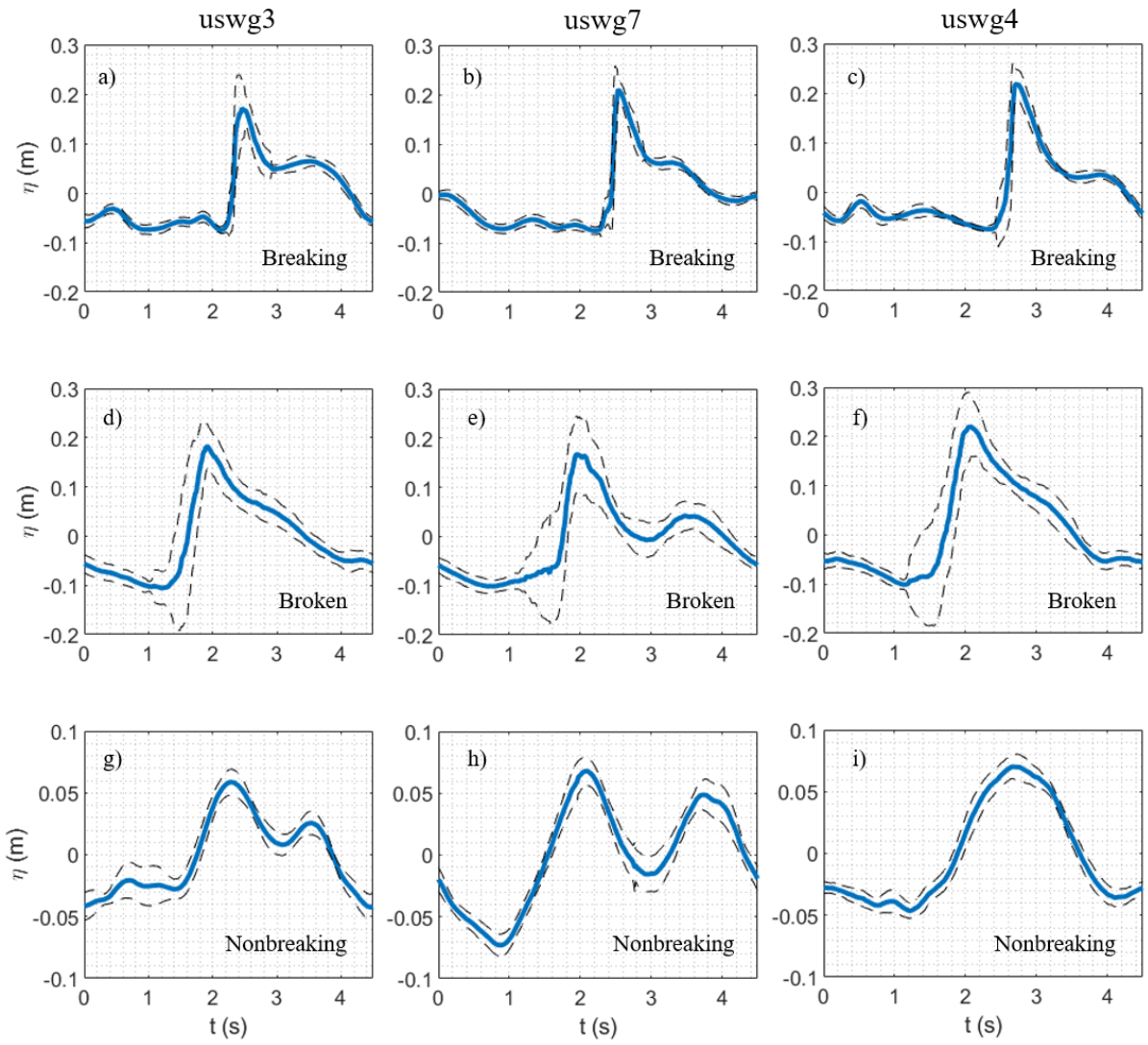

Figure 8. Examples of ensemble-averaged free surface elevations (blue solid line) from Trial 7 (a, b, and c, h_0 = 1.30 m), Trial 18 (d, e, and f, h_0 = 1.40 m), and Trial 19 (g, h, and i, h_0 = 1.45 m) and their standard deviations (black dashed line). Plots on the left (a, d, and g) were taken from uswg3; plots in the middle (b, e, and h) were taken from uswg7; plots on the right (c, f, and i) were taken from uswg4.

Table 5. Ensemble averaged wave heights calculated from wg1, wg2, uswg3, uswg7, and uswg4 (m).

Trial	h_0 (m)	H_{in} (m)	T (s)	wg1 (m)	wg2 (m)	uswg3 (m)	uswg7 (m)	uswg4 (m)
1	1.10	0.1	4.5	0.12	0.10	0.09	0.07	0.11
2	1.10	0.4	4.5	0.54	0.49	0.08	0.11	0.12
3	1.12	0.1	4.5	0.12	0.12	n/a	n/a	n/a
4	1.20	0.2	4.5	0.18	0.21	0.14	0.14	0.15
5	1.20	0.3	4.5	0.33	0.37	0.18	0.18	0.18

6	1.30	0.1	4.5	0.14	0.11	0.16	0.20	0.16
7	1.30	0.2	4.5	0.25	0.24	0.24	0.28	0.29
8	1.30	0.3	4.5	0.33	0.32	0.25	0.25	0.27
9	1.30	0.3	3.5	0.29	0.34	0.19	0.20	0.19
10	1.30	0.3	5.5	0.36	0.40	0.26	0.20	0.23
11	1.35	0.1	4.5	0.11	0.13	0.16	0.13	0.18
12	1.35	0.2	4.5	0.19	0.22	0.35	0.33	0.41
13	1.35	0.3	4.5	0.30	0.28	0.32	0.30	0.31
14	1.35	0.4	4.5	n/a	0.37	0.27	0.27	0.31
15	1.40	0.1	4.5	0.12	0.09	0.16	0.13	0.11
16	1.40	0.2	4.5	n/a	0.20	0.32	0.30	0.30
17	1.40	0.3	4.5	0.32	n/a	0.36	0.38	0.39
18	1.40	0.4	4.5	0.38	n/a	0.29	0.27	0.32
19	1.45	0.1	4.5	0.13	0.08	0.10	0.14	0.12
20	1.45	0.2	4.5	0.20	0.16	0.25	0.27	0.27
21	1.45	0.3	4.5	0.27	n/a	0.37	0.38	0.40

It is important to classify the types of waves that were run during the experiment and to know when it is acceptable to apply specific wave theories. Figure 9 shows the classification of the types of waves run for each trial of the experiment at wg1 and uswg7 except for Trial 3, where H is the ensemble averaged wave height, h is the still water depth, and L is the calculated wavelength. Filled circles are for wg1, which was offshore, and hollow circles are for uswg7 in front of the on-grade specimen. The marker types correspond to the still water depth at the wavemaker at the start of each trial. For this experiment, second order nonlinear waves were generated and can be classified as Cnoidal waves. At wg1, most waves are within the Cnoidal Theory limits and are in shallow water based on Fenton's limit. Waves from approximately four trials can be classified by linear wave theory in intermediate water depth. At uswg7, all waves are defined by Cnoidal waves and are in shallow water. These waves are all either approaching the theoretical breaking limit given by Miche's equation or have crossed the theoretical breaking limit.

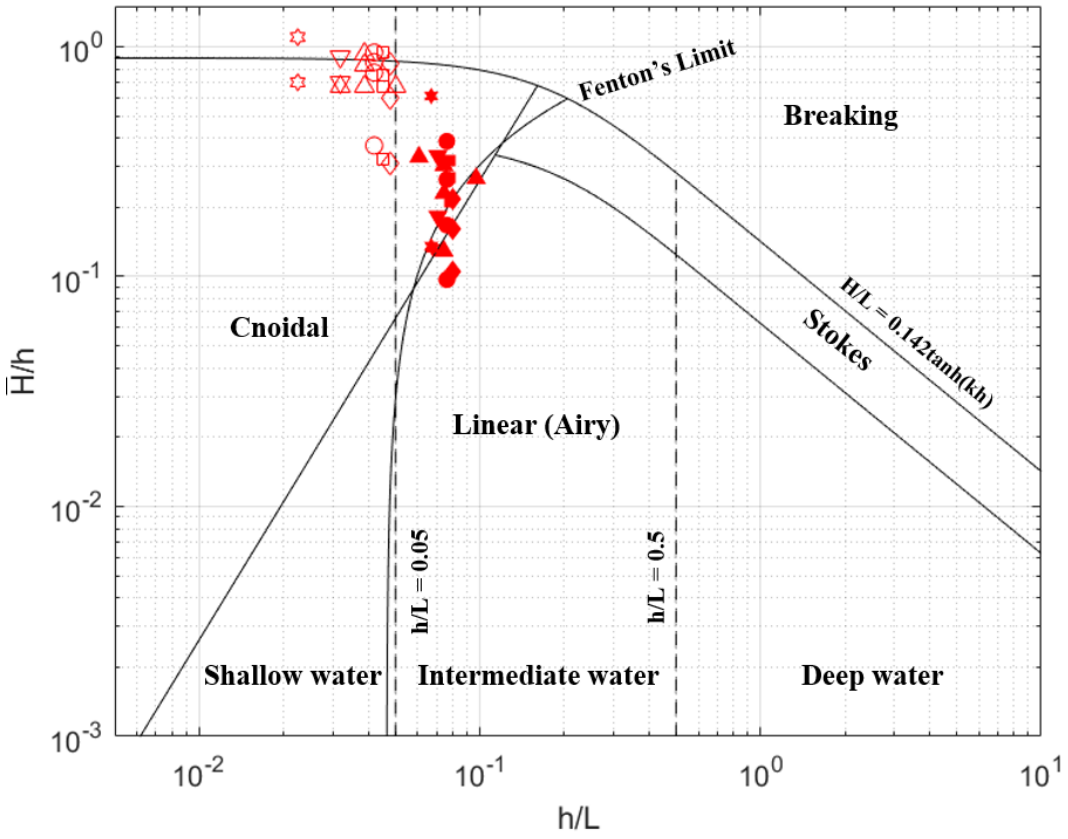

Figure 9. Wave classification from wg1 (solid) and uswg7 (hollow) for each trial. For h_0 = 1.10 m (star); h_0 = 1.20 m (downward triangle); h_0 = 1.30 m (upward triangle); h_0 = 1.35 m (circle); h_0 = 1.40 m (square); h_0 = 1.45 m (diamond).

Figure 10 shows the ensemble-averaged uplift pressures, P_u, from four of the twelve total pressure sensors and the total vertical force per unit width, F_v, taken from the eight pressure sensors along the middle of the elevated specimen from Trial 18. The magnitude of the uplift pressures is consistent with Park et al. (2017). The peak pressure decreases and becomes more elongated as the wave moves through the structure, which was present for a majority of trials. F_v was calculated by integrating the pressure distribution over the length of the specimen in the x-direction.

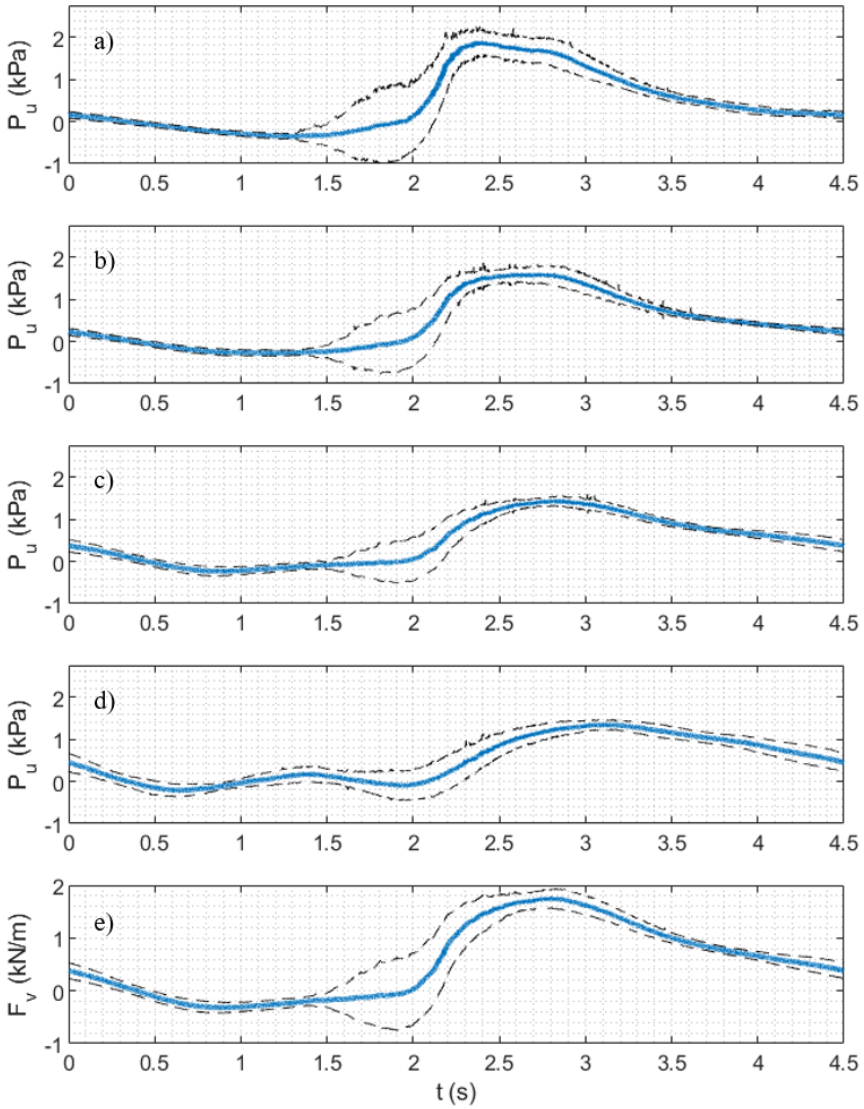

Figure 10. Ensemble averaged uplift pressures and total vertical force measured on the elevated specimen from press1 (a), press5 (b), press7 (c), press10 (d), and total vertical force (e) from Trial 18 (h_0 = 1.40 m).

6. Results

6.1. Description of progressive damages and failure

The first goal of this project was to design and construct specimens that behaved similarly to full-scale wood-frame residential structures and to create hydrodynamic conditions where these specimens would fail similar to their full-scale counterparts observed in previous field studies (Kennedy et al. 2011; Tomiczek et al. 2017; Hatzikyriakou et al. 2015). Trial 1 had a local water depth of 0.10 m and was already flooding the first level of the on-grade specimen. Wall panels started to disconnect from the on-grade

specimen during the first trial and continued to do so until failure. Figure 11 is a photo of the specimens during Trial 10, where multiple wall panels disconnected from the on-grade specimen. The on-grade specimen failed at a local water depth of 0.35 m (2.1 m prototype). The input wave height was 0.20 m, and an ensemble-averaged wave height of 0.35 m (2.1 m prototype) was measured at the specimens.

These waves were breaking directly on the specimens with relatively large forces. Table 4 indicates that the on-grade specimen had experienced 461 cumulative waves (N_{WO}) throughout the 12 trials. N_{WO} was calculated by identifying the number of waves that created a force on the on-grade specimen that exceeded 10% of the peak force measured by load cell 1 throughout the 12 trials. The first story of the specimen, where the waves were impacting, failed in shear, causing the specimen to detach from its foundation. At the instant the on-grade specimen failed, the elevated specimen remained standing with minor damage. Results in Table 4 indicate that the elevated specimen only experienced 289 cumulative waves (N_{WE}) at the end of Trial 12. N_{WE} was calculated by identifying the number of waves that created a vertical pressure on the elevated specimen that exceeded 10% of the peak pressure measured by pressure sensor 1 throughout the 21 trials.

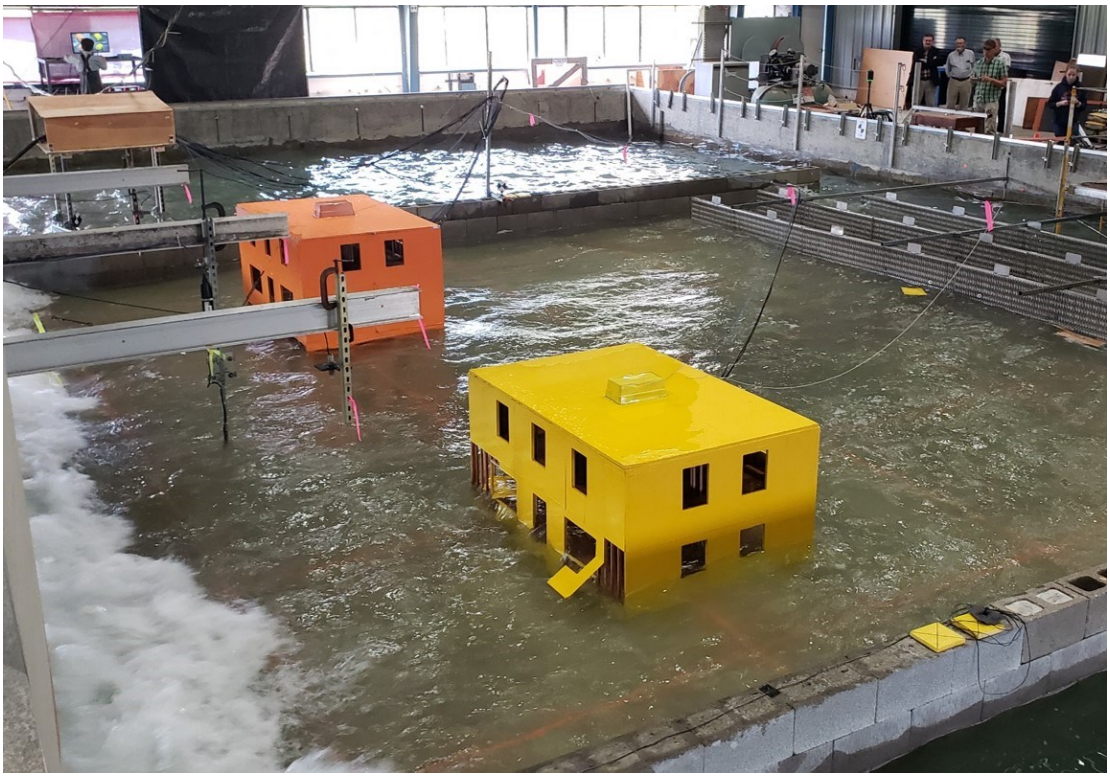

Figure 11. Photo taken during trial 10 (h_0 = 1.30 m that shows the damages the specimens experienced during testing.

Similarly, to the on-grade specimen, wall panels began disconnecting from the elevated specimen once the water depth reached 0.35 m and the first level of the elevated specimen was inundated. The elevated specimen failed at a local water depth of 0.45 m (2.7 m prototype) at the specimen, which corresponds to an air gap of -0.10 m. Table 4 indicates that the specimen experienced a total of 620 waves before failing. The input wave height was 0.30 m and an ensemble-averaged wave height of 0.40 m (2.4 m prototype) was measured at the specimen. Similarly to Trial 12, when the on-grade specimen failed, these waves were breaking directly on the elevated specimen.

Both specimens failed at the expected water levels and in ways very similar to what was observed in the field based on the observations of Hatzikyriakou et al. (2015), Kennedy et al. (2011), and Tomiczek et al. (2013, 2017). Both specimens failed at the first floor and were disconnected from their foundations. Because of these experimental observations of comparable hydrodynamic conditions to Hurricane Sandy

noted earlier, the experiments can be considered to have successfully reproduced well, qualitatively, the progressive damage and failure of wood-frame residential structures under hurricane surge and wave conditions.

6.2. Progressive damage analysis using LiDAR

LiDAR scans were taken of the wave basin before Trial 1 (presurvey scan) and before each increase in water level. Point clouds generated from the scans were used to quantitatively and qualitatively track the progressive damages of each specimen. Yu et al. (2019) used Leica Cyclone to model the structural members of each specimen, including each wall panel and wall stud. Figure 12 and Figure 13 show the models that were created of both specimens from each scan. These figures show the progressive damages to the walls that were discussed in Section 6.1. Points below the water level and areas of the specimen that were covered in water were not visualized because the scanners used do not scan through the water.

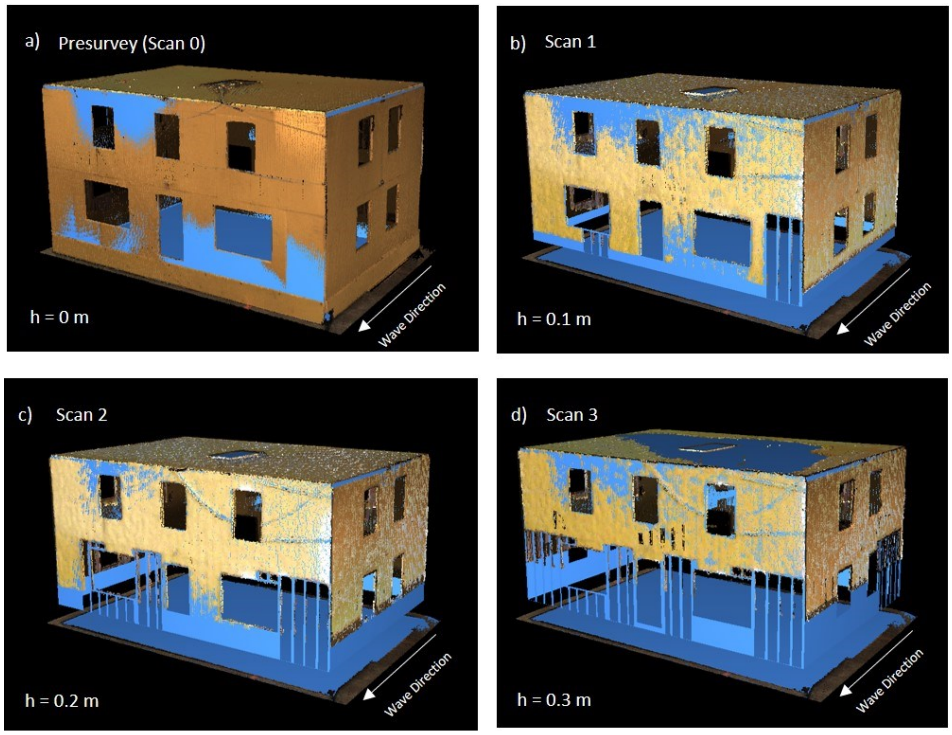

Figure 12. Models of the on-grade specimen created after each scan (Yu et al., 2019).

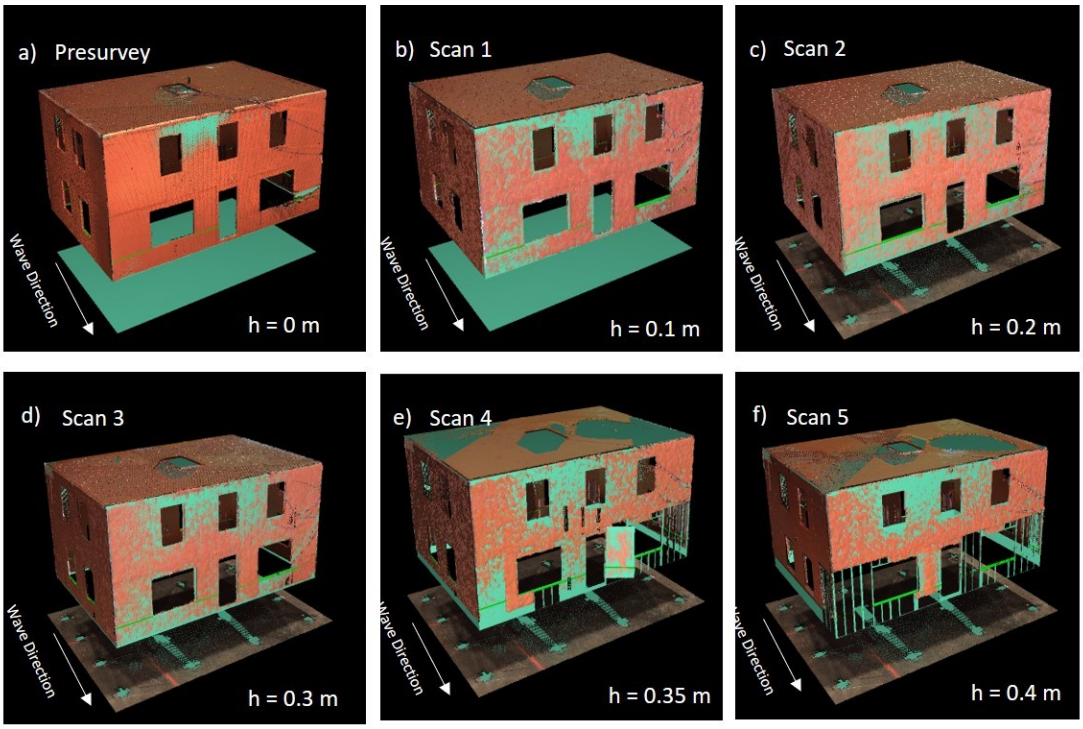

Figure 13. Models of the elevated specimen created after each scan (Yu et al., 2019).

The LiDAR scans of the specimens taken before Trial 1 were compared to the scans taken before each increase in water level. Yu et al. (2019) created a cumulative damage fraction, *c'*, that is used to calculate the fraction of cumulative wall damage each specimen experienced leading up to the current scan:

$$c' = \text{Cumulative Damage Fraction} = \frac{\text{Presurvey Wall Area- Scan \# Wall Area}}{\text{First Floor Presurvey Wall Area}^{*}} \quad (2).$$

Figure 14a and Figure 14b show *c'* as a function of water depth, *h*, in the *x*-direction and *y*-direction, respectively. As expected, the on-grade specimen was damaged at lower water depths before the elevated specimen experienced any damage. The parameter *h'* was developed to compare the damage rates between the specimens. This parameter is a measurement of the still water depth relative to the elevation of the bottom of the wall panels for each specimen. The elevation of the bottom of the wall panels on the on-grade specimen was found to be 0.108 m. The elevation of the bottom of the wall panels on the elevated specimen was found to be 0.343 m. Therefore, *h'* can be calculated as

$$h' = h - 0.108m \quad (3)$$

for the on-grade specimen and

$$h' = h - 0.343m \quad (4)$$

for the elevated specimen. Figure 14c and Figure 14d show *c'* as a function of *h'* in the *x*-direction and *y*-direction. These plots also indicate that the elevated specimen failed at a slightly quicker rate than the on-grade specimen. The difference in damage rates may be because the elevated specimen became waterlogged and structurally weaker the longer it was in the water and experienced more waves relative to the on-grade specimen.

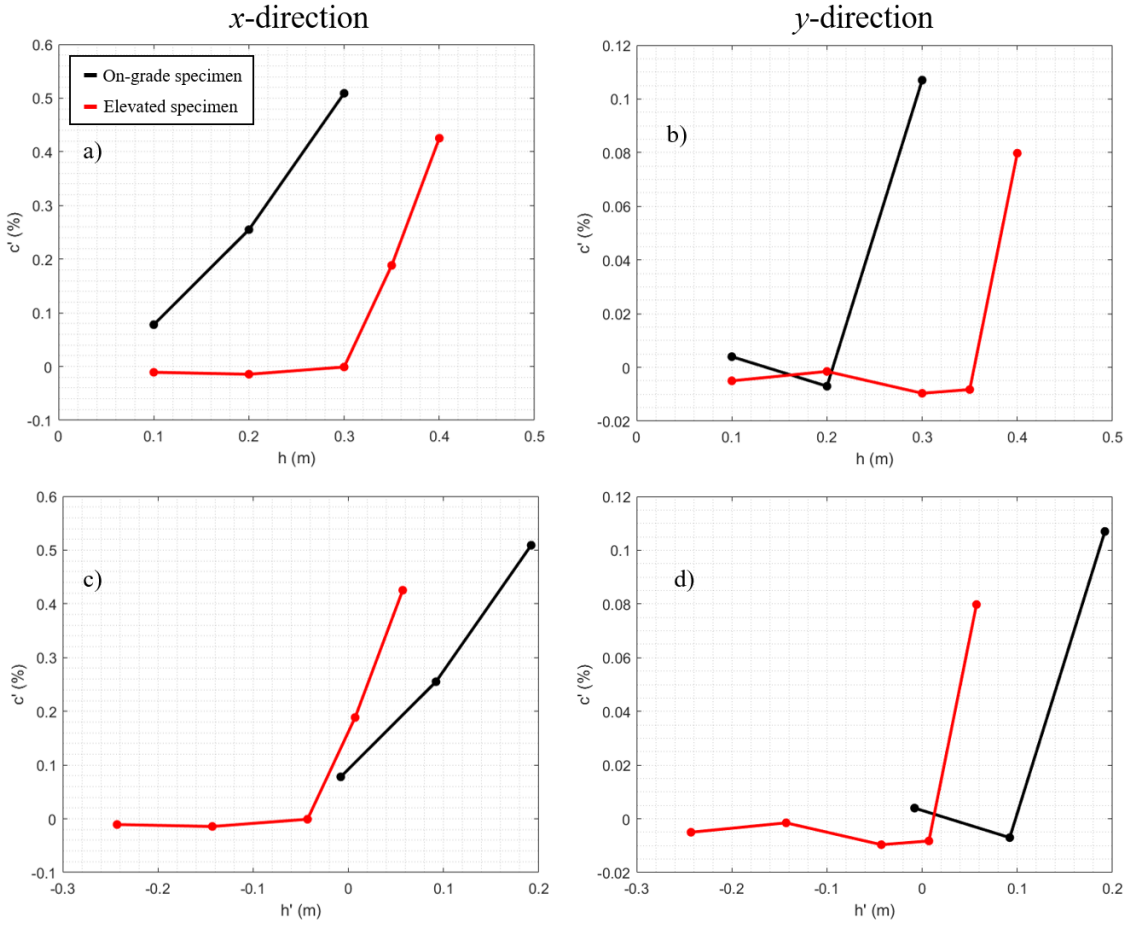

Figure 14. Cumulative damage fraction, c', of the on-grade specimen (red) and elevated specimen (black) as a function of h (a, b) and h' (c, d). Panels a and c are of walls oriented in the x-direction and panels b and d are of walls oriented in the y-direction (Yu et al., 2019).

Yu et al. (2019) also quantitatively tracked the damages of the specimens using a damage state classification system. The classification, shown in Table 6, is a modification of the system used in Tomiczek

et al. (2017). The damage states range from 0 to 4, where 0 indicates no visible damage and 4 indicates that the walls of the specimen were disconnected. Figure 15 shows the damage state of the walls oriented in the *x*-direction for each specimen as a function *h'* created by Yu et al. (2019). This figure also shows the higher rate of damage of the elevated specimen. It is noted that the walls oriented in the *y*-direction were not classified into damage states because of the low damage fractions of these walls.

Table 6. Damage state classification system (Yu et al., 2019).

Damage state				
0	1	2	3	4
• No visible damage	• < 15% damage to normally oriented walls • loose or partially removed panels	• > 15% cumulative damage to normally oriented walls	• > 40% cumulative damage to normally oriented walls	• Walls have collapsed

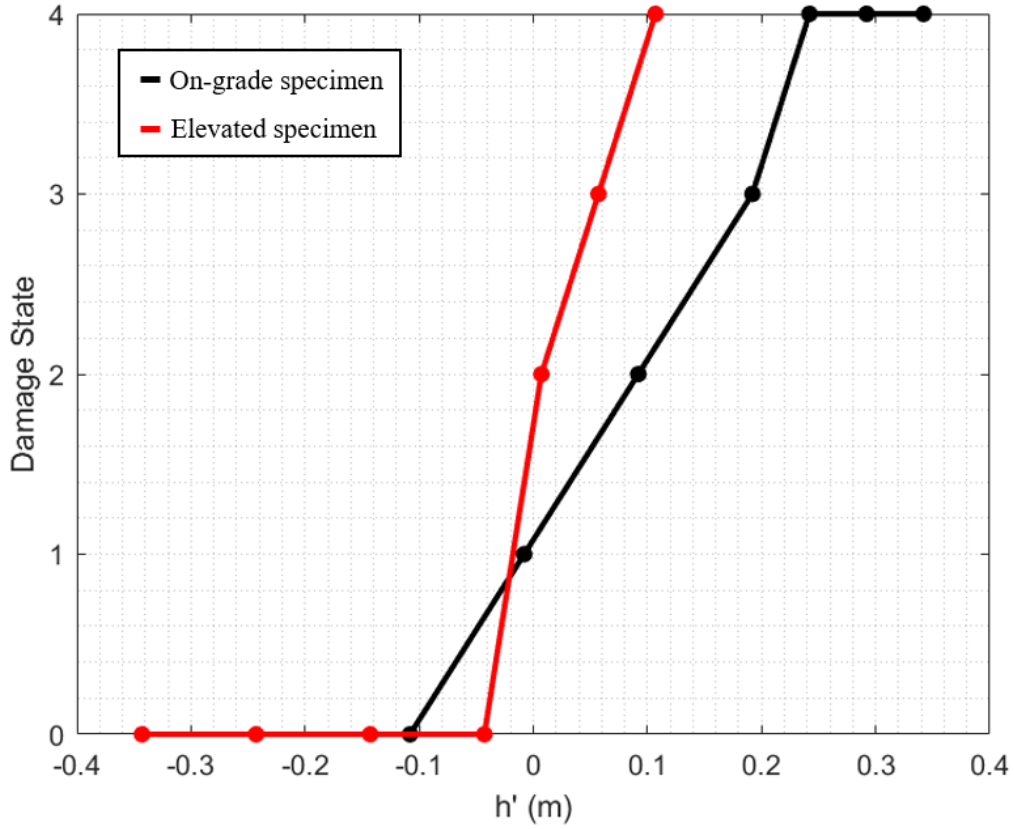

Figure 15. Damage state of the on-grade specimen (black) and the elevated specimen (red) as a function of h' (Yu et al., 2019).

As expected, Figure 14 shows that the on-grade specimen experienced damage at lower water depths and ultimately failed before the elevated specimen. However, Figure 15 indicates that the elevated specimen experienced damage rates higher than the on-grade specimen. The results shown in this section also show that LiDAR scans of a physical laboratory model can be used to track progressive damage quantitatively.

6.3. In-water Damage Identification

Figure 16 shows acceleration measurements and corresponding power spectrum density (PSD) functions for obtained from the hydrodynamic testing for trials 2 and 13, to illustrate the data collected. In each subfigure, plots are shown for responses in the x-direction and y-direction. In Figure 16a and b, it can be seen that the amplitude of the accelerations recorded in Trial 13 were considerably larger than those

recorded in Trial 2, which was expected since the wave height recorded at uswg7 (near the structure) were 0.11 m and 0.30 m for trial 2 and 13, respectively. In Figure 16b, it can also be seen that the amplitude of the accelerations in the x-direction are notably higher than the ones in the y-direction. Note also that the first 20 seconds (approximately) are not plotted for the time series, since this was prior to arrival of the waves to the structure and that the acceleration data are differentiated into four groups, each one represented with a different color.

Figure 16c and d show the power spectrum functions for trials 2 and 13, respectively, for both the x- and y-directions. Note that the colors of the PSD functions shown have direct relation to the colors selected in plotting of the acceleration time series for the same trials and for the x- and y-directions. The frequencies at which the peak values of the PSD functions are observed correspond to the natural frequencies. Comparison of the natural frequencies obtained from Figure 16c (Trial 2) and d (Trial 13) indicate that the natural frequencies in both the x- and y-direction tend to decrease with increase trial number.

The reduction in natural frequencies as a function of the trial number can be further observed in Figure 17, which shows the identified natural frequencies as a function of the trial number for the elevated specimen. For each trial, four points are shown in this figure for both the x-direction and y-direction markers, which correspond to the four groups of waves mentioned in results shown in Figure 16. The reduction of the natural frequency with trial number can in part be explained with the accumulated loss of shear walls that was observed during testing that was also illustrated in Section 6.2. The natural frequency reduction can also be attributed to the loosening of nails and other connections and other load duration effects on wood members and connections (e.g., Rosowsky and Bulleit, 2002). However, this was not explored further in this study.

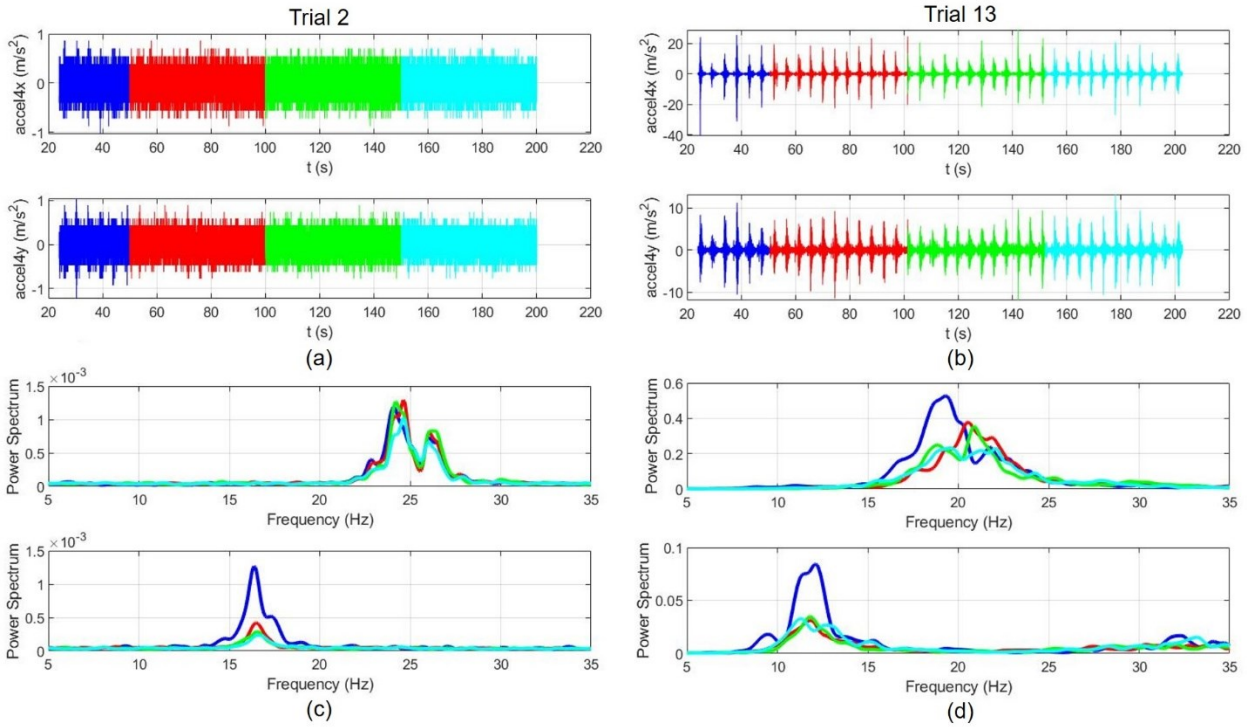

677

678 Figure 16. Elevated specimen hydrodynamic testing response in terms of *x*- and *y*-direction. Acceleration
679 measurements for (a) Trial 2 (h_0 = 1.10 m) and (b) Trial 13 (h_0 = 1.35 m). Corresponding power spectrum
680 for (c) Trial 2 and (c) Trial 13. Note that approximately the first 20 seconds were not considered in the
681 data analysis reported here and that colors of the curves for the power spectral density functions shown
682 have direct relation to the colors selected in plotting of the acceleration time series.

683

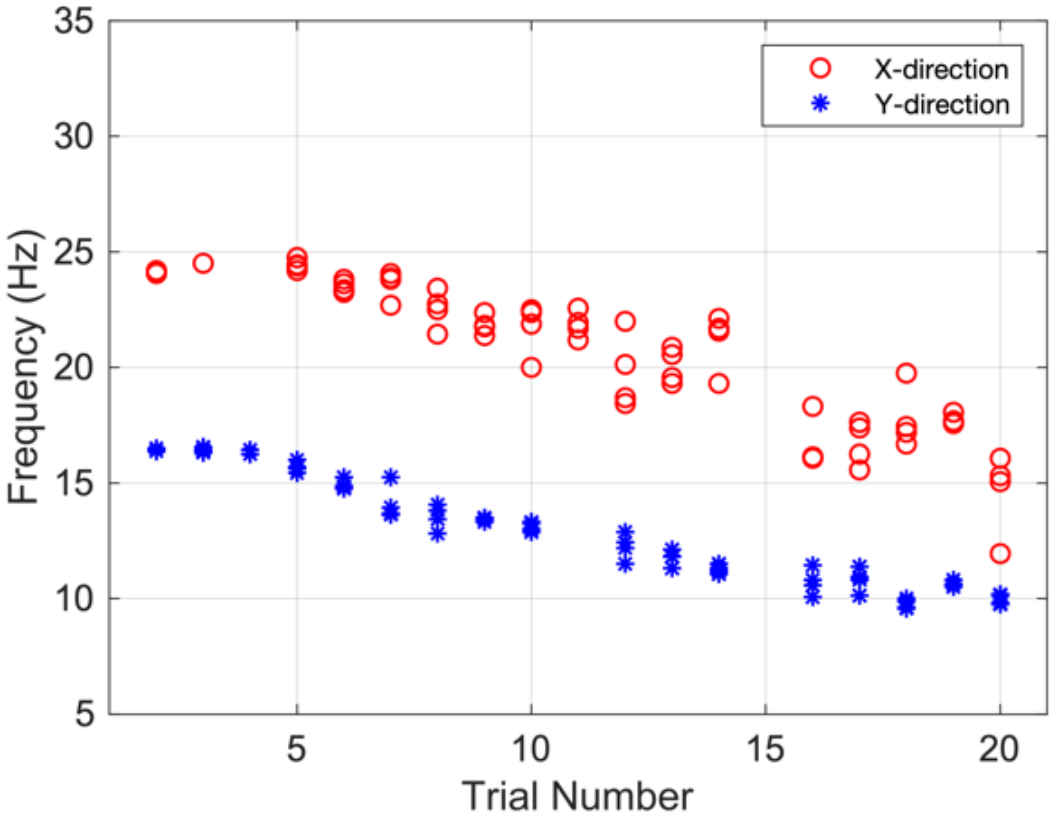

Figure 17. Elevated specimen identified natural frequency as a function of the trial number.

6.4. Pressure distribution on the elevated specimen

Pressure sensors were also installed in the alongshore (*y*-direction) on the bottom front (press1, press2, and press3) and back (press10, press11, and press12) of the elevated specimen to determine the variation in the *y*-direction (Figure 5). Table 7 shows the uplift pressure measured at pressure sensors 1, 2, and 3 ($P_{u,1}$, $P_{u,2}$, and $P_{u,3}$) and the standard deviation and standard error of the three sensors during the time of maximum ensemble-averaged vertical force, $t_{v,max}$. Table 7 also shows the uplift pressure of pressure sensors 10, 11, and 12 ($P_{u,10}$, $P_{u,11}$, and $P_{u,12}$) and the standard deviation and standard error of the three sensors during $t_{v,max}$. The variation in pressure in the *y*-direction was small and, therefore, was considered negligible for the vertical force calculations that will be discussed in Section 6.5 and Section 6.6.

Table 7. Uplift pressures during time of maximum vertical force and the standard deviation (σ) and standard error (SE).

Trial	$P_{u,1}$ (kPa)	$P_{u,2}$ (kPa)	$P_{u,3}$ (kPa)	σ (kPa)	SE (kPa)	$P_{u,10}$ (kPa)	$P_{u,11}$ (kPa)	$P_{u,12}$ (kPa)	σ (kPa)	SE (kPa)
1	n/a	n/a	n/a	n/a	n/a	n/a	n/a	n/a	n/a	n/a
2	n/a	n/a	n/a	n/a	n/a	n/a	n/a	n/a	n/a	n/a
3	n/a	n/a	n/a	n/a	n/a	n/a	n/a	n/a	n/a	n/a
4	n/a	n/a	n/a	n/a	n/a	n/a	n/a	n/a	n/a	n/a
5	n/a	n/a	n/a	n/a	n/a	n/a	n/a	n/a	n/a	n/a
6	0.60	0.47	0.43	0.07	0.04	-0.08	-0.13	-0.22	0.06	0.03
7	0.24	0.12	0.27	0.07	0.04	0.47	0.45	0.53	0.03	0.02
8	0.67	0.54	0.70	0.07	0.04	0.82	0.72	0.57	0.10	0.06
9	0.83	0.77	0.88	0.05	0.03	0.26	0.22	0.12	0.06	0.03
10	0.84	0.69	0.81	0.06	0.04	0.32	0.27	0.12	0.09	0.05
11	0.86	0.69	0.66	0.09	0.05	0.19	0.15	0.01	0.08	0.04
12	1.11	0.91	0.94	0.09	0.05	0.36	0.31	0.21	0.06	0.03
13	1.12	0.98	1.06	0.06	0.03	0.85	0.80	0.84	0.02	0.01
14	1.40	1.24	1.28	0.07	0.04	1.02	1.00	1.03	0.01	0.01
15	0.71	0.58	0.77	0.08	0.04	0.96	0.98	0.99	0.01	0.01
16	1.74	1.45	1.65	0.12	0.07	1.10	1.03	0.92	0.07	0.04
17	1.48	1.37	1.50	0.06	0.03	1.20	1.19	1.32	0.06	0.03
18	1.64	1.67	1.66	0.01	0.01	1.22	1.19	1.20	0.01	0.01
19	1.81	1.66	1.75	0.06	0.04	1.24	1.23	1.20	0.02	0.01
20	2.54	2.84	2.58	0.13	0.08	1.00	0.89	0.78	0.09	0.05
21	2.04	2.37	2.03	0.16	0.09	1.67	1.66	1.74	0.04	0.02

As previously mentioned, pressure sensors were aligned down the center of the elevated specimen to observe the variation in uplift pressure the specimen experienced in the *x*-direction. Figure 18 shows the uplift pressure distribution on the elevated specimen during the $t_{v,max}$, during trials 18, 19, 20, and 21. The $t_{v,max}$ for trials 18,19, 20, and 21 are 2.81 s, 2.82 s, 2.66 s, and 2.60 s, respectively. Each bar represents is the ensemble averaged pressure measured during $t_{v,max}$ by the eight pressure sensors aligned down the center of the elevated specimen (press1, press4-press10). The bar positioned at x' = 0.04 m is the ensemble averaged uplift pressure measured by press1 and the bar positioned at x' = 1.17 m is the ensemble averaged pressure measured by press10.The uplift pressure distribution for these trials is linearly decreasing from the front to the back of the specimen, which was observed for most trials with a negative air gap. While the maximum uplift pressure is not always at the very front of the specimen, it is likely that it will occur near

the front. This indicates that the uplift pressures will be greatest at the front of the structure and will decrease as a wave travels from the front to the back of a structure for waves that produce relatively large vertical forces.

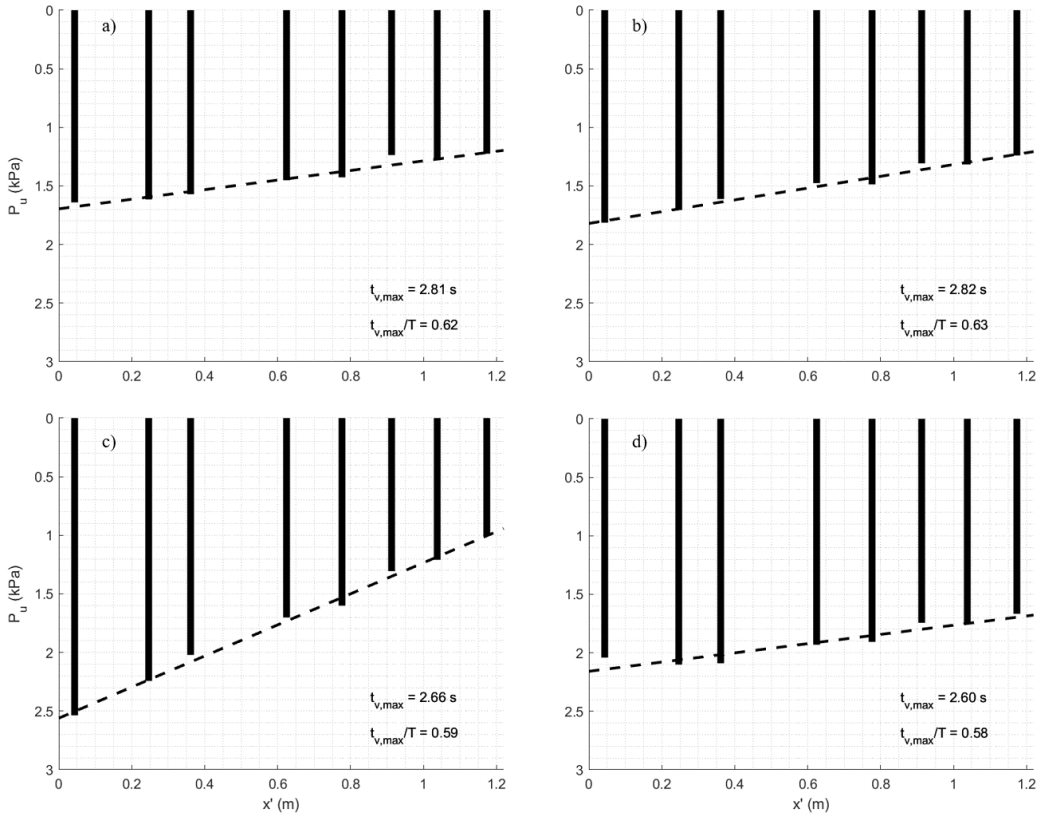

Figure 18. Uplift pressure distribution along the bottom of the elevated specimen at the time of maximum vertical force during trials 18 (a, h_0 = 1.40 m), 19, (b, h_0 = 1.45 m), 20 (c, h_0 = 1.45 m), and 21 (d, h_0 = 1.45 m). *x*' indicates the location of the pressure sensor measurement relative to the length of the specimen in the wave direction (*x*-direction).

6.5. Vertical forces on the elevated specimen

The ensemble-averaged vertical force (F_v) was found on the elevated specimen for each trial by integrating the pressure distribution measured by the sensors along the bottom of the specimen. For this to be done, the measured pressures were assumed to be constant over a horizontal distance that extended halfway between adjacent sensors. The pressure measured by each sensor was then integrated over this distance to obtain a force acting on that section of the specimen. These forces were then added together to

obtain a total vertical force time series. Finally, the time series was ensemble-averaged and the maximum force, $F_{v,max}$, was identified. Figure 19 shows $F_{v,max}$ for each trial plotted as a function of the ensemble-averaged wave height, $\overline{H}$, at uswg4 in front of the elevated specimen. The different colors indicate nonbreaking (blue), broken (black), and breaking (red) waves. The various marker types indicate a water depth of 0.30 m (triangles), 0.35 m (circles), 0.40 m (squares), and 0.45 m (diamonds). Figure 19 shows a correlation between increasing wave height and increasing vertical force, which is consistent with past literature such as Bradner et al. (2011). There are two outlier trials where the wave heights were relatively small (approximately $\overline{H}$ = 0.11m) yet yielded relatively large forces. The air gap is negative in these two outlier trials, which could explain why the measured force is larger than expected with small wave heights.

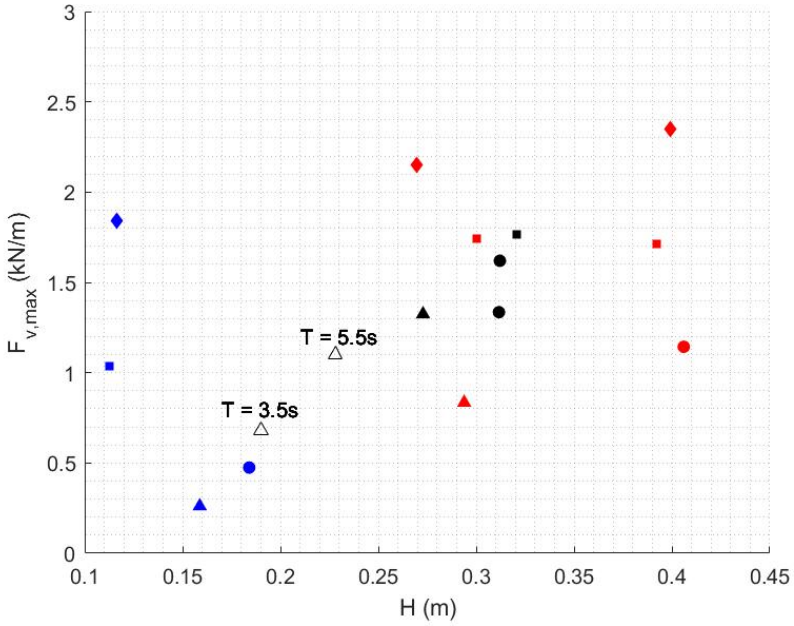

Figure 19. Maximum ensemble-averaged vertical force against ensemble-averaged wave height. Colors indicate nonbreaking (blue), broken (black), and breaking (red) waves. Marker types indicate trials where h = 0.30 m (triangles), h = 0.35 m (circles), h = 0.40 m (squares), and h = 0.45 m (diamonds).

Figure 20 shows $F_{v,max}$ plotted as a function of the air gap, a. The different marker types indicate a value of $\overline{H}$ less than 0.15 m (stars), between 0.15 m and 0.25 m (downward triangle), between 0.25 m and 0.35 m (upward triangles), and greater than 0.35 m (circles). Figure 20 shows the maximum vertical force

742 is significantly affected by the air gap. The trials with the greatest ensemble-averaged forces all occurred
743 during the trials with the largest negative air gap. Past literature has indicated that the vertical forces are
744 usually at a maximum when a is zero (Bradner et al., 2011; Park et al., 2017; Sogut et al., 2020; Tomiczek
745 et al., 2019). The reason why this differs from our experiment could be due to the floor beams and girders
746 on the underside of the elevated specimen to follow building codes discussed in Section 3. In addition,
747 previous experiments, such as Park et al. (2017) and Tomiczek et al. (2019), used repeated input wave
748 conditions at various air gaps causing the same wave types and wave breaking locations throughout the
749 experiment. In this study, the wave conditions and breaking locations varied for each air gap condition
750 which could also explain the difference in vertical force readings. Past literature has also indicated that the
751 vertical forces will begin to decrease as the air gap becomes more negative because the bottom of the
752 structure is less affected by the dynamic pressures (Park et al., 2017; Tomiczek et al., 2019). However, the
753 elevated specimen failed before more trials could be run, so this effect is not present in this study.
754 Nonbreaking waves had the smallest force at each of the different air gaps due to relatively small wave
755 heights, but at the most negative air gap, a nonbreaking wave produced a relatively large force compared
756 to all other trials even with a small wave height. The peak forces occurring at an air gap of -0.1 m were due
757 to relatively large waves breaking on the specimen directly. All trials had a period of T = 4.5 s except for
758 Trial 9 and Trial 10, which are labeled in both plots and indicated by hollow markers. Bradner et al. (2011)
759 found that the maximum uplift force was dependent on the wave period. Not enough data was collected to
760 see any significant trends in wave period and vertical force, which is a characteristic that could be studied
761 in future experiments.

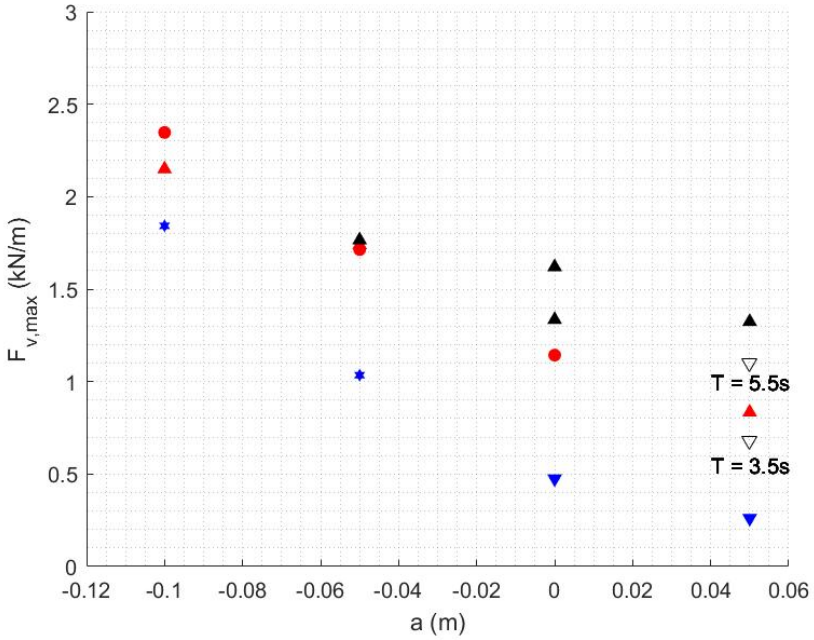

Figure 20. Maximum ensemble averaged vertical force against air gap. Nonbreaking (blue), broken (black), and breaking (red). $\overline{H} < 0.15$ m (stars), 0.15 m $\leq \overline{H} < 0.25$ m (down triangle), 0.25 m $\leq \overline{H} < 0.35$ m (triangles), and $\overline{H} \geq 0.35$ m (circles).

6.6. Predictive uplift pressure distribution equation

The second goal of this study was to develop an uplift pressure distribution equation for the elevated specimen. As mentioned previously, there is a lack of design criteria for uplift pressures and forces in current design manuals such as the CCM and ASCE 7-16. Although uplift equations exist for caisson structures (Goda, 1974), these structures have a rubble-mound base, so these equations are not directly applicable. Because this present experiment conducted only a limited number of trials because of the destructive nature of the tests, the data set is not sufficient to develop a comprehensive formula. However, because there are relatively few experiments on residential structures in shallow water under surge and wave conditions, it is worthwhile to investigate the general form of the equation.

Based on the observations of Figure 18, the general form of the uplift pressure distribution equation is a linear line of the form:

$$P_u = P_{u,0} + mx' \quad (5),$$

where P_u is the pressure distribution along the centerline of the bottom of the structure, $P_{u,0}$ is the uplift pressure at the front edge of the bottom of the structure, m is the slope in kPa/m, and x' is the position on the bottom surface of the structure in the x-direction, where positive is onshore and in the direction of wave propagation. Equation 5 is a line with a maximum value at the leading edge (x' = 0 m) and decreasing shoreward, as can be seen in the dashed lines in Figure 18. This line fit the measured uplift pressure distributions during trials where the maximum vertical force, $F_{v,max}$, was relatively large. Because of this, trials where $F_{v,max}$ exceeds 1.18 kN/m, which is 50% of the maximum force measured for all trials, were only considered when calculating m and $P_{u,0}$. The value of m was found by averaging the slopes of the fitted uplift pressure distribution lines (Figure 18) for trials where the maximum vertical force exceeded 1.18 kN/m. The average slope was m = -0.4 kPa/m.

Cuomo et al. (2007) developed predictive force equations dependent on wave crest elevation, air gap, and water depth since these parameters were correlated to vertical forces. Earlier work and the data collected from this experiment showed that wave height and air gap are correlated with vertical force, therefore the parameter α was developed in this study to include wave height and air gap in the calculation of $P_{u,0}$ which is:

$$\alpha = \bar{H} - a \tag{6}.$$

The intercept of each fitted pressure distribution lines for where $F_{v,max}$ > 1.18 kN/m were plotted as a function of α and the intercepts were found to be positively correlated to α. A linear line was fitted through these data points and the equation of this line was set equal to $P_{u,0}$. $P_{u,0}$ was calculated as

$$P_{u,0} = 0.64 + 3.0\alpha \tag{7}.$$

Equation 7 was substituted into the general form of the uplift pressure distribution equation (Equation 5) to obtain:

$$P_u = 0.64 + 3.0\alpha - 0.4x' \tag{8}.$$

Since the development of this equation was only considered for trials where $F_{v,max}$ exceeded 50% of the maximum force measured for all trials, Equation 8 is only valid for certain ranges of $\bar{H}$, a, h and structure

804 length, w, to wavelength, L, ratios. The range of $\overline{H}$ is between 0.12 m and 0.39 m, the range of a is between
805 -0.10 m and 0.05 m, the range of h is between 0.30 m and 0.45 m, and the range of w to L is between 0.13
806 and 0.16. The ranges of $\overline{H}$, a, and h translate to 0.72 m and 2.34 m, -0.54 m and 0.30 m, and 1.8 m and 2.7
807 m, respectively when the 1:6 experimental length scale is considered.

808 Equation 8 must be integrated over the length of the structure in the x-direction to obtain the total
809 vertical force. Figure 21 shows the maximum vertical force, $F_{v,max}$, as a function of α. This figure shows the
810 positive correlation between maximum vertical force and α. A conservative uplift pressure distribution
811 equation was also created:

812 $$P_u = 1.1 + 3.0\alpha - 0.4x' \quad (9).$$

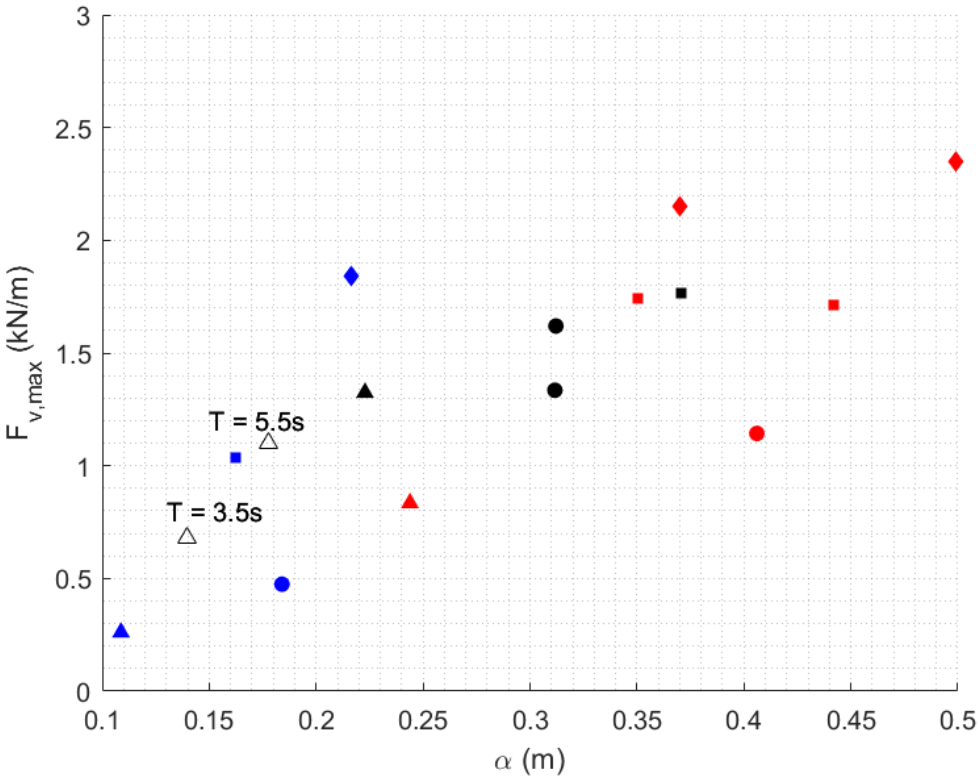

813

814 Figure 21. Maximum vertical force as a function of α. Colors indicate nonbreaking (blue), broken (black),
815 and breaking (red) waves. Marker types indicate trials where h = 0.30 m (triangles), h = 0.35 m (circles), h
816 = 0.40 m (squares), and h = 0.45 m (diamonds).

817

818

819 Equation 9 was created by adding an additional 0.46 to $P_{u,0}$ to ensure the equation would over predict the
820 vertical force for every trial during the experiment.

821 Figure 22 compares the measured vertical forces and predicted vertical forces using both Equation
822 8 and Equation 9. Solid circles indicate the trials where the maximum vertical force exceed 50% of the
823 highest $F_{v,max}$ value recorded and hollow circles indicate trials where the maximum vertical force did not
824 exceed 50% of the highest $F_{v,max}$ value recorded and therefore did not have ranges of $\bar{H}$, a, h, and w to L in
825 the valid ranges described above.

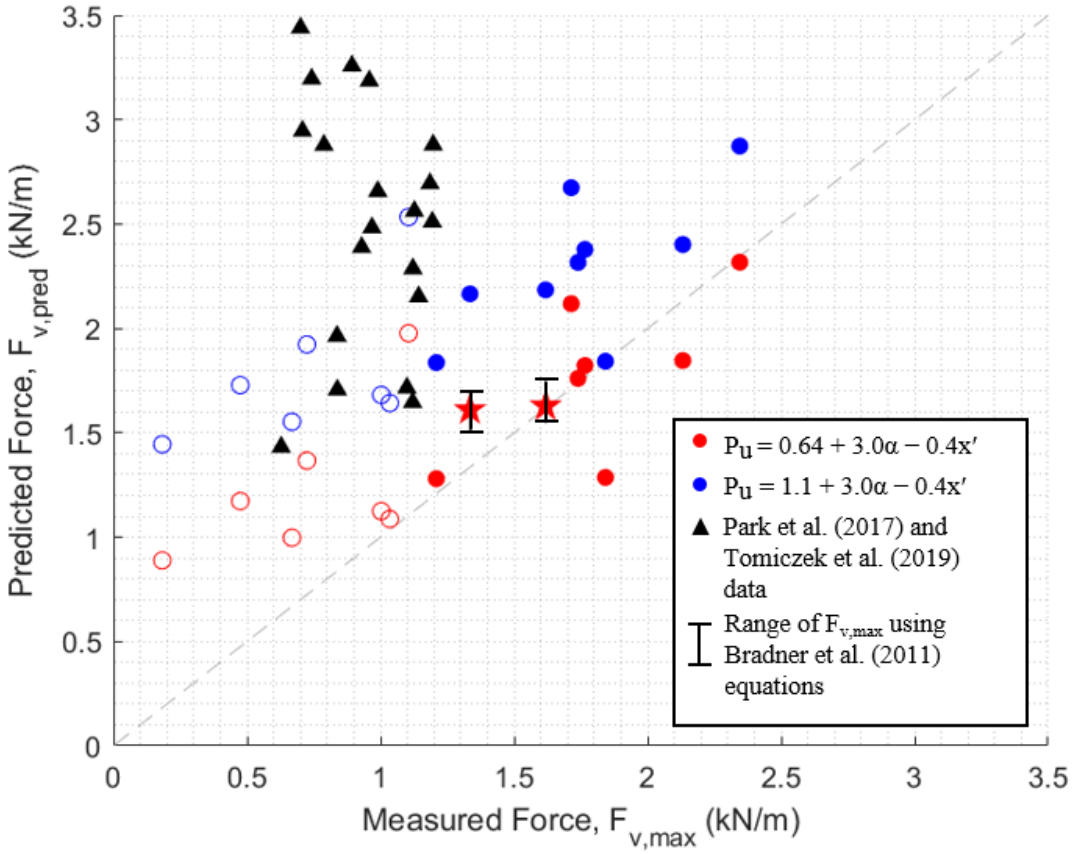

826

827 Figure 22. Measured vertical force compared to the predicted vertical force. Force predicted using Equation
828 8 in red and force predicted using Equation 9 in blue. A marker that is not filled indicates that the trial did
829 not use values of $\bar{H}$, a, h, and w to L within the valid ranges described above.

830

831 Data from Park et al. (2017) and Tomiczek et al. (2019) was used in conjunction with the data
832 collected from this study to validate Equation 8 and Equation 9. Figure 22 also shows the comparison of

the measured vertical force from Park et al. (2017) and Tomiczek et al. (2019) (black triangles) and the predicted vertical force after integrating Equation 8. Equation 8 seems to over predict the measured vertical force from the experiments done by Park et al. (2017) and Tomiczek et al. (2019).

Brander et al. (2011) also created predictive equations from their experimental study for both vertical and horizontal forces. The researchers developed force equations for many of the water depths and periods they tested with regular waves, ending up with 29 vertical force equations dependent on wave height. Two of the 29 equations were developed using parameters within the valid ranges of Equation 8 in this study. The equations are:

$$F_v = 1.47H + 58.2H^2 \tag{10}$$

and

$$F_v = 9.58H + 24.4H^2 \tag{11},$$

where H is the measured wave height and F_v is the measured vertical force. These equations were developed using trials where a = 0 m and, therefore, can only be used to predict the vertical force on the elevated specimen in this study for Trials 13 and 14, where a is also 0 m. Figure 22 also compares of the predicted vertical force using Equations 10 and 11 and the measured vertical force from this study. This figure shows that the predicted vertical force that is calculated using Equation 8 during Trials 13 and 14 (red stars) is within the range of the predicted vertical force that is calculated using the equations developed by Bradner et al. (2011). This shows that developing an equation for vertical forces that is dependent on wave height and the air gap is possible.

7. Discussion

The results of this study indicate that the modeled specimens behaved similarly to full-scale residential structures when exposed to surge and waves. The specimens in this study were constructed as rectangular idealized wood-frame coastal residences. However, the geometries of real-world coastal residences vary significantly, and different building archetypes should be studied, such as the specimens constructed in Wilson et al. (2008) including the effects of overhanging structural members. The girders

858 and floor joists constructed on the bottom side of the elevated specimen added a level of complexity to the
859 vertical pressures and forces. A similar wood-frame structure without these structural members should be
860 exposed to similar surge and wave conditions to quantitatively compare the effects the structural members
861 have on the vertical pressures and forces such as air entrainment. The specimens were also constructed with
862 openings to represent windows and doors on a residential structure. These openings can significantly affect
863 the forces on a structure. These openings will decrease the area of impact but also allows water to rush
864 through the structure causing large forces in the inside of the structure on the back walls.

865 Pressure sensors were only installed on the bottom of the elevated specimen to measure uplift
866 pressures, and load cells were only installed underneath the on-grade specimen. Pressure sensors mounted
867 on the front face of the specimens should be considered to compare horizontal and vertical pressures and
868 forces similarly to Park et al. (2017). Additional pressure sensors installed on the bottom side of the elevated
869 specimen in a grid would allow for the pressure distribution in both the x-direction and y-direction to be
870 more accurately measured. Additional load cells could be installed on the elevated specimen for additional
871 force measurements in both the horizontal and vertical directions.

872 Regular waves were considered in this study for simplicity and to easily identify the wave heights
873 and water depths that caused the specimens to fail. However, irregular waves are more realistic and would
874 expose the specimens to conditions similar to the real world. In a future study, a hydrograph of Hurricane
875 Sandy conditions could be used to replicate the wave climate during the storm. Additionally, this study
876 considered only one wave period (4.5 s) except for two trials. Bradner et al. (2011) found that the wave
877 period is positively correlated to wave forces due to larger wave celerity and wave energy flux, so the effect
878 of wave period should be taken into consideration in alternative studies.

879 The uplift pressure equation developed in this study was only valid for a specific range of structure
880 length to wavelength ratios, air gaps, wave heights, and water depths. These ranges are 0.13 to 0.16, -0.10
881 m to 0.05 m, 0.12 m to 0.39 m, and 0.30 m to 0.45 m, respectively. Future studies should consider increasing
882 the boundaries of these ranges to cover a larger range of values. In addition to increasing the parameter
883 boundaries, uplift pressure equations should consider breaking types. Figure 20 shows the effects of wave

884 breaking types and wave breaking locations have on vertical forces. Developing equations for specific
885 breaking types will increase the accuracy of the uplift pressure distribution equation. Bradner et al. (2011)
886 and Sogut et al. (2020) also found that the momentum flux is highly correlated to maximum forces on
887 elevated structures. This should also be explored to increase the accuracy of predictive uplift force
888 equations.

889 **8. Conclusion**

890 This study used regular waves with varying wave heights and water depths to test the performance
891 and behavior of 1:6 scale wood-frame on-grade and elevated residential house specimens. The following
892 conclusions were found from this study:

893 1. Through careful design and construction, a scaled wood-frame specimen was constructed to behave
894 and fail under wave forcing conditions similar to full-scale residential structures with similar
895 structural properties and forcing.
896 2. LiDAR was shown to be a useful tool to track the progressive damage of laboratory specimens
897 quantitatively.
898 3. The on-grade specimen experienced damages at lower water depths compared to the elevated
899 structure as expected.
900 4. The elevated specimen experienced higher rates of damages than the on-grade specimen when
901 compared at the same elevation of the structure due to the increased wave heights at the elevated
902 specimen.
903 5. Vertical forces on the elevated specimen are correlated with wave height, air gap, and water depth.
904 Vertical forces were found to increase with increasing wave heights and water depth. Previous
905 studies have shown that maximum vertical forces occur when the bottom of the lowest horizontal
906 member (LHM) of an elevated structure is even with the still water level. In this study, the peak
907 vertical forces occurred at the greatest water depths during the maximum submergence of the

specimens. Previous laboratory studies mentioned in this paper did not consider waves entering the specimen through openings and did not include floor joists on the bottom of the specimen.

6. Vertical forces are also affected by breaking type and location. Waves breaking directly on the specimens generally caused larger vertical forces.
7. An empirical uplift pressure distribution equation (Equation 8) was developed dependent on wave height and air gap. The equation is valid for a specific range of structure length to wavelength ratios, wave heights, air gaps, and water depths, which are 0.13 to 0.16, 0.12 m to 0.39 m, -0.10 m to 0.05 m, and 0.30 m to 0.45 m, respectively. The equation is conservative when comparing it to other data sets such as Park et al. (2017) and Tomiczek et al. (2019) and agrees with the vertical force equations developed by Bradner et al. (2011). This shows that developing an equation for vertical forces that is dependent on wave height and the air gap is possible.

This study increases the current work to better understand the wave-structure interaction during hurricane storm conditions. Through more work, the design criteria of residential structures can be improved to increase the resiliency of coastal communities to extreme storm events.

9. Acknowledgments

The material in this study is based upon work partially supported by the US Department of Homeland Security under award No. 2015-ST-061-ND0001-01 and by the National Science Foundation under awards 1519679 and 1661315. Any opinions, findings, and conclusions or recommendations expressed in this material are those of the authors and do not necessarily reflect the views of the Department of Homeland Security or the National Science Foundation. The authors would like to thank the technical staff at the NSF-funded NHERI facility. In addition, the authors would like to thank Ignace Mugabo for performing the ambient and forced vibration testing and data analyses for that dataset, Erzhuo Che and Dae Kun Kang for operating the LiDAR, and Michael Olsen for assistance with the use of Cyclone.

931 **References**

932 Alam, M. S., Winter, A. O., Galant, G., Shekhar, K., Barbosa, A. R., Motley, M. R., Eberhard,
933 M. O., Cox, D. T., Arduino, P., and Lomonaco, P. (2020). Tsunami-Like Wave-Induced
934 Lateral and Uplift Pressures and Forces on an Elevated Coastal Structure. *Journal of*
935 *Waterway, Port, Coastal and Ocean Engineering*, *146*(4).
936 https://doi.org/10.1061/(ASCE)WW.1943-5460.0000562

937 ATC. (2017) Recommended Modeling Parameters and Acceptance Criteria for Nonlinear
938 Analysis in Support of Seismic Evaluation, Retrofit, and Design. *National Institute of*
939 *Standards and Technology*. doi: 10.6028/NIST.GCR.17-917-45.

940 ASCE. (2016). *Minimum Design Loads and Associated Criteria for Buildings and Other*
941 *Structures*. Reston, VA.

942 Barbosa, A.R., Fahnestock, L.A., Fick, D.R., Gautam, D., Soti, R., Wood, R., Moaveni, B.,
943 Stavridis, A., Olsen, M.J., and Rodrigues, H., (2017). "Performance of Medium-to-High
944 Rise Reinforced Concrete Frame Buildings with Masonry Infill in the 2015 Gorkha Nepal
945 Earthquake." Earthquake Spectra. Earthquake Spectra: December 2017, Vol. 33, No. S1,
946 pp. S197-S218. https://doi.org/10.1193/051017EQS087M

947 Blake, E. S., and Gibney, E. J. (2008). The Deadliest, Costliest, and Most Intense United States
948 Tropical Cyclones from 1851 to 2010 (and Other Frequently Requested Hurricane Facts).
949 In *NOAA Technical Memorandum NWS NHC-6* (Vol. 53, Issue 9).
950 https://doi.org/10.1017/CBO9781107415324.004

951 Blake, E. S., Kimberlain, T. B., Berg, R. J., Cangia, Losi, J. P., and Beven II, J. L. (2013).
952 Tropical cyclone report Hurricane Sandy (AL182012) 22 – 29 October 2012.
953 https://doi.org/10.1017/CBO9781107415324.004

954 Bradner, C., Schumacher, T., Cox, D., and Higgins, C. (2011). Large-scale laboratory
955 measurements of wave forces on highway bridge superstructures. *Proceedings of the*
956 *Coastal Engineering Conference*, 3554–3566.

957 Burke, J. (2018). *Structural Testing of a 1:6 Scaled, Light-frame Construction, Near-coastal,*
958 *Residential Structure*. MS Thesis, Oregon State University, Corvallis, USA.

959 Chopra, A. K. (1995). *Dynamics of Structures*. Prentice-Hall. Englewood Cliffs, New Jersey.

960 Cox, D., Arikawa, T., Barbosa, A., Guannel, G., Inazu, D., Kennedy, A., ... and Roueche, D.
961 (2019). Hurricanes Irma and Maria post-event survey in US Virgin Islands. Coastal
962 Engineering Journal, 61(2), 121-134.

963 Cuomo, G., Tirindelli, M., and Allsop, W. (2007). Wave-in-deck loads on exposed jetties.
964 *Coastal Engineering*, *54*(9), 657–679. https://doi.org/10.1016/j.coastaleng.2007.01.010

965 Eamon, C. D., Fitzpatrick, P., and Truax, D. D. (2007). Observations of Structural Damage
966 Caused by Hurricane Katrina on the Mississippi Gulf Coast. *Journal of Performance of*
967 *Constructed Facilities*, *21*(2), 117–127. https://doi.org/10.1061/(asce)0887-

968 3828(2007)21:2(117)

969 Elsner, J. B., Trepanier, J. C., Strazzo, S. E., and Jagger, T. H. (2012). Sensitivity of limiting
970 hurricane intensithy to ocean warmth. *Geophysical Research Letters*, 39(17), 1-6.
971 https://doi.org/10.1029/2012GL053002

972 FEMA. (2011). Determining Site-Specific Loads. In *Coastal Construction Manual* (pp. 5–27).
973 Washington, DC.

974 Garcia, R. A. (2008). *Wave and Surge Loading on Light-Frame Wood Structures*. MS Thesis,
975 Colorado State University, Fort Collins, CO, USA.

976 Duncan, S. (2020). *Physical Modeling of Progressive Damage and Failure of Wood-Frame*
977 *Coastal Residential Structures Due to Waves and Surge Forces*. MS Thesis, Oregon State
978 University, Corvallis, OR, USA.

979 Goda, Y. (2010). *Random Seas and Design of Maritime Structures* (3rd Edition). World
980 Scientific.

981 Goda, Y. (1974). New Wave Pressure Formulae for Composite Breakwaters. *Proc. 14Th. Asce*
982 *Coastal Engng. Conf. (Copenhagen, Denmark)*, *3*((JUNE 24-28, 1974)), 1702–1720.
983 https://doi.org/10.9753/icce.v14.100

984 Hatzikyriakou, A., Lin, N., Gong, J., Xian, S., Hu, X., and Kennedy, A. (2015). Component-
985 Based Vulnerability Analysis for Residential Structures Subjected to Storm Surge Impact
986 from Hurricane Sandy. *Natural Hazards Review*, *17*(1), 1–15.
987 https://doi.org/10.1061/(ASCE)NH.1527-6996.0000205

988 Kaplan, P. (1979). Impact forces on horizontal members of an offshore test structure. *Proc. of*
989 *Civ. Eng. in the Oceans IV*, 716–731.

990 Kaplan, P., Murray, J. J., and Yu, W. C. (1995). Theoretical Analysis of Wave ImpactForces
991 on Platform Deck Structures. *Offshore Technology OMAE*, 189–198.

992 Karny, M. (2018). *Hydrodynamic Testing on a 1:6 Scale, Wood Framed Near-Coast*
993 *Residential Structure*. MS Thesis, Oregon State University, Corvallis, USA.

994 Kennedy, A., Rogers, S., Sallenger, A., Gravois, U., Zachry, B., Dosa, M., and Zarama, F.
995 (2011). Building Destruction from Waves and Surge on the Bolivar Peninsula during
996 Hurricane Ike. *Journal of Waterway Port Coastal and Ocean Engineering*, *137*(132),
997 132–141. https://doi.org/10.1061/(ASCE)WW

998 Koliou, M., van de Lindt, J. W., and Hamburger, R. O. (2018). Nonlinear Modeling of Wood-
999 Frame Shear Wall Systems for Performance-Based Earthquake Engineering:
1000 Recommendations for the ASCE 41 Standard. Journal of Structural Engineering, 144(8),
1001 04018095

1002 Lindt, J. W. van de, Gupta, R., Cox, D. T., and Wilson, J. S. (2009). Wave Impact Study on a
1003 Residential Building. *Journal of Disaster Research*, *4*(6), 419–426.
1004 https://doi.org/10.20965/jdr.2009.p0419

Linton, D., Gupta, R., Cox, D., Van De Lindt, J., Oshnack, M. E., and Clauson, M. (2013). Evaluation of tsunami loads on wood-frame walls at full scale. *Journal of Structural Engineering (United States)*, *139*(8), 1318–1325. https://doi.org/10.1061/(ASCE)ST.1943-541X.0000644

Mansard, E. and Funke, E. (1980). The Measurement of Incident and Reflected Spectra Using a Least Squares Method. *Proceedings of the 17th Conference on Coastal Engineering*, pp. 154-172.

Moaveni, B., Barbosa, A. R., Conte, J. P., and Hemez, F. M. (2014). Uncertainty analysis of system identification results obtained for a seven-story building slice tested on the UCSD-NEES shake table. *Structural Control and Health Monitoring*, *21*(4), 466-483.

Morison, J. R., Johnson, J. W., and Schaaf, S. A. (1950). The Force Exerted by Surface Waves on Piles. *Petroleum Transactions*, *189*, 149–154.

Mosqueda, G., Porter, K. A., O'Connor, J., and McAnany, P. (2007). Damage to Engineered Buildings and Bridges in the Wake of Hurricane Katrina. 1–11. https://doi.org/10.1061/40943(250)4

NOAA and NHC. (2018). Costliest US tropical cyclones tables updated. *NOAA Technical Memorandum NWS NHC-6*, 3. https://www.nhc.noaa.gov/pdf/nws-nhc-6.pdf%0Ahttps://www.nhc.noaa.gov/news/UpdatedCostliest.pdf%0Ahttps://www.nhc.noaa.gov/pdf/nws-nhc-6.pdf%0Ahttps://www.nhc.noaa.gov/dcmi.shtml

Park, H., Tomiczek, T., Cox, D. T., van de Lindt, J. W., and Lomonaco, P. (2017). Experimental modeling of horizontal and vertical wave forces on an elevated coastal structure. *Coastal Engineering*, *128*(2017), 58–74. https://doi.org/10.1016/j.coastaleng.2017.08.001

Prevatt, D. O., Roueche, D. B., Aponte-Bermúdez, L. D., Kijewski-Correa, T., Li, Y., Chardon, P., Cortes, M., López del Puerto, C., Mercado, A., Muñoz, J., and Morales, A. (2018). Performance of Structures under Successive Hurricanes: Observations from Puerto Rico and the U.S. Virgin Islands after Hurricane Maria. *Forensic Engineering*, 1049-1059.

Robertson, I. N., Riggs, H. R., Yim, S. C., and Young, Y. L. (2007). Lessons from Hurricane Katrina Storm Surge on Bridges and Buildings. *Journal of Waterway, Port, Coastal, and Ocean Engineering*, *133*(6), 463–483. https://doi.org/10.1061/(asce)0733-950x(2007)133:6(463)

Rosowsky, D. V., & Bulleit, W. M. (2002). Load duration effects in wood members and connections: order statistics and critical loads. *Structural Safety*, 24(2-4), 347-362.

Sarpkaya, T., and Isaacson, M. (1981). *Mechanics of wave forces on offshore structures*. Van Nostrand Reinhold Co.

Sogut, E., Velioglu Sogut, D., and Farhadzadeh, A. (2020). Overland Wave Propagation and Load Distribution among Arrays of Elevated Beachfront Structures. *Journal of Waterway, Port, Coastal, and Ocean Engineering*, *146*(4), 04020016. https://doi.org/10.1061/(asce)ww.1943-5460.0000579

Takahashi, S., Tanimoto, K., and Simosako, K. (1994). A proposal of impulsive pressure coefficient for the design of composite breakwaters. *Proc. Int. Conf. Hydro-Technical Eng. for Port and Harbor Constr*.

Tomiczek, T., Kennedy, A., and Rogers, S. (2013). Collapse Limit State Fragilities of Wood-Framed Residences from Storm Surge and Waves during Hurricane Ike. *Journal of Waterway, Port, Coastal, and Ocean Engineering*, *140*(1), 43–55. https://doi.org/10.1061/(asce)ww.1943-5460.0000212

Tomiczek, T., Kennedy, A., Zhang, Y., Owensby, M., Hope, M. E., Lin, N., and Flory, A. (2017). Hurricane Damage Classification Methodology and Fragility Functions Derived from Hurricane Sandy's Effects in Coastal New Jersey. *Journal of Waterway, Port, Coastal, and Ocean Engineering*, *143*(5), 04017027. https://doi.org/10.1061/(asce)ww.1943-5460.0000409

Tomiczek, T., Wyman, A., Park, H., and Cox, D. T. (2019). Modified Goda Equations to Predict Pressure Distribution and Horizontal Forces for Design of Elevated Coastal Structures. *Journal of Waterway, Port, Coastal and Ocean Engineering*, *145*(6), 1–16. https://doi.org/10.1061/(ASCE)WW.1943-5460.0000527

Wiebe, D. M., Park, H., and Cox, D. T. (2014). Application of the Goda pressure formulae for horizontal wave loads on elevated structures. *KSCE Journal of Civil Engineering*, *18*(6), 1573–1579. https://doi.org/10.1007/s12205-014-0175-1

Wilson, J. S. (2008). *Behavior of a 1/6th Scale, Two-Story, Wood Framed Residential Structure Under Surge Wave Loading*. MS Thesis, Oregon State University, Corvallis, USA.

Wilson, J. S., Gupta, R., van de Lindt, J. W., Clauson, M., & Garcia, R. (2009). Behavior of a one-sixth scale wood-framed residential structure under wave loading. Journal of Performance of Constructed Facilities, 23(5), 336-345.

Wood, R. L., Mohammadi, M. E., Barbosa, A. R., Abdulrahman, L., Soti, R., Kawan, C. K., and Olsen, M. J. (2017). Damage assessment and modeling of the five-tiered pagoda-style Nyatapola temple. Earthquake Spectra, 33(1_suppl), 377-384.

Yeh, S. C., Rogers Jr., S. M., Tung, C. C., and Kasal, B. (1999). Behavior of Breakaway Walls under Wave Action. *Journal of Structural Engineering*, *125*(October), 1162–1169.

Yu, C., Cox, D., Barbosa, A.R., Che, E., Duncan, S., Tomiczek, T. (2019). Progressive Damage Assessment of On-Slab and Elevated Structures from Storm Surge and Waves Using LiDAR in a Laboratory Wave Basin. Undergraduate Research Experience (REU) Report. NHERI 2019: DesignSafe-CI. https://doi.org/10.17603/ds2-0rky-9w25.

Yu, H., Mohammed, M.A., Mohammadi, M.E., Moaveni, B., Barbosa, A.R., Stavridis, A., Wood, R.L. (2017). Structural Identification of an 18-story RC Building in Nepal Using Post-Earthquake Ambient Vibration Data. Frontiers in Built Environment, section Structural Sensing, https://doi.org/10.3389/fbuil.2017.00011